The Pennsylvania State University

The Graduate School

DETECTION OF DEFECTS IN SILICON CARBIDE PIN DIODES VIA ELECTRICALLY DETECTED MAGNETIC RESONANCE

A Thesis in

Engineering Science and Mechanics

by

William R. Barker

Submitted in Partial Fulfillment
of the Requirements
for the Degree of

Master of Science

December 2020

The thesis of William Barker was reviewed and approved by the following:

Patrick Lenahan
Distinguished Professor of Engineering Science and Mechanics
Thesis Advisor

Mark Horn
Professor of Engineering Science and Mechanics

Michael Lanagan
Professor of Engineering Science and Mechanics
Associate Director, Materials Research Institute
Associate Director, Center for Dielectric Studies

Judith Todd
Department Head of Engineering Science and Mechanics
P. B. Breneman Chair
Professor of Engineering Science and Mechanics

Abstract

Silicon carbide PIN diodes were investigated via X-band electrically detected magnetic resonance spectroscopy. The devices were studied under two different modulation frequencies, 12,500 Hz and 100 Hz. A g map of these results shows an anisotropic g for the centerline. Both the side features found in the 100 Hz data set and the spectra detected suggest that the dominating spin-dependent defect is similar to nitrogen-related defects in previous silicon carbide electrically detected magnetic resonance and electron paramagnetic resonance investigations. The defect or defects present likely involve an intrinsic paramagnetic center and almost certainly also involves a deep level impurity center, but the exact nature of the defect or defects requires further investigation. The 100 Hz data reveals side peaks not present in the higher modulation frequency measurements. This fundamentally different frequency response of the two EDMR spectra suggests a complex EDMR response. One possible explanation is that charge carriers tunnel to shallow, near-interface oxide defects near the edges of the diode before tunneling back. This is supported by the idea that one spin-dependent process is slower than spin dependent recombination.

Table of Contents

List of Figures v

Acknowledgements vii

1 Introduction 1

2 Literature Review 3
- 2.1 Electron Paramagnetic Resonance 3
- 2.2 Electrically Detected Magnetic Resonance 5
- 2.3 Electron Paramagentic Resonance Results in SiC Devices 7

3 Methods 13

4 Results 16
- 4.1 $\theta = 0°$ 17
- 4.2 $\theta = 15°$ 18
- 4.3 $\theta = 30°$ 19
- 4.4 $\theta = 45°$ 20
- 4.5 $\theta = 60°$ 21
- 4.6 $\theta = 75°$ 22
- 4.7 $\theta = 90°$ 23
- 4.8 $\theta = 105°$ 24
- 4.9 $\theta = 120°$ 25
- 4.10 $\theta = 135°$ 26
- 4.11 $\theta = 150°$ 27
- 4.12 $\theta = 165°$ 28

5 Discussion 29
- 5.1 General Discussion 29
- 5.2 12,500 Hz 32
- 5.3 100 Hz 36

6 Summary and Conclusion 40

7 Bibliography 42

List of Figures

2.1 A simple illustration of spin dependent trap assisted tunneling. D1 and D2 represent trap locations, B1 is the quasistatic magnetic field, and the diagram otherwise uses conventional band diagram notation. In a), the tunneling event is forbidden, whereas in b) it is allowed because the charge carrier spin has been flipped at the resonance condition. Figure from [1]. 6
2.2 EDMR results on PN diodes that a) have n++ implantation and b) do not have n++ implantation. Figure from [2]. 9
2.3 ESE results for subtitional nitrogen in 4H-SiC. While not explicitly reported, the centerline has about $g = 2.006$. Figure from [3]. 10
2.4 $N_x$defect in heavily doped n-type 4H SiC at a) 15K and b) at 70 K. Figure from [4]. 11

3.1 Schematic of an EDMR spectrometer. Note that the electromagnet schematic in the figure does not include all of the components featured on the spectrometer used in this work. Figure from [5]. 14
3.2 Schematic for the SiC PIN diode most similar to that used in this work. Note that the exact dimensions of the PIN used in this work are not necessarily the same or similar to this figure. The figure should only be used to have an understanding of what the PIN is like. Figure from [6]. 15

4.1 Data at $\theta = 0°$ and a modulation frequency of 12,500 Hz. 17
4.2 Data at $\theta = 0°$ and a modulation frequency of 100 Hz. 17
4.3 Data at $\theta = 15°$ and a modulation frequency of 12,500 Hz. 18
4.4 Data at $\theta = 15°$ and a modulation frequency of 100 Hz. 18
4.5 Data at $\theta = 30°$ and a modulation frequency of 12,500 Hz. 19
4.6 Data at $\theta = 30°$ and a modulation frequency of 100 Hz. 19
4.7 Data at $\theta = 45°$ and a modulation frequency of 12,500 Hz. 20
4.8 Data at $\theta = 45°$ and a modulation frequency of 100 Hz. 20
4.9 Data at $\theta = 60°$ and a modulation frequency of 12,500 Hz. 21
4.10 Data at $\theta = 60°$ and a modulation frequency of 100 Hz. 21
4.11 Data at $\theta = 75°$ and a modulation frequency of 12,500 Hz. 22
4.12 Data at $\theta = 75°$ and a modulation frequency of 100 Hz. 22
4.13 Data at $\theta = 90°$ and a modulation frequency of 12,500 Hz. 23
4.14 Data at $\theta = 90°$ and a modulation frequency of 100 Hz. 23
4.15 Data at $\theta = 105°$ and a modulation frequency of 12,500 Hz. 24
4.16 Data at $\theta = 105°$ and a modulation frequency of 100 Hz. 24
4.17 Data at $\theta = 120°$ and a modulation frequency of 12,500 Hz. 25

4.18 Data at $\theta = 120°$ and a modulation frequency of 100 Hz. 25
4.19 Data at $\theta = 135°$ and a modulation frequency of 12,500 Hz. 26
4.20 Data at $\theta = 135°$ and a modulation frequency of 100 Hz. 26
4.21 Data at $\theta = 150°$ and a modulation frequency of 12,500 Hz. 27
4.22 Data at $\theta = 150°$ and a modulation frequency of 100 Hz. 27
4.23 Data at $\theta = 165°$ and a modulation frequency of 12,500 Hz. 28
4.24 Data at $\theta = 165°$ and a modulation frequency of 100 Hz. 28

5.1 Composite figure of all central gs. 30
5.2 EDMR traces from SiC/SiO_2 interfaces in MOS devices. Figure from [7]. 31
5.3 Magnitude of the peak-to-peak signal at each angle for each modulation frequency. This plot is inherently normalized by current insofar as the measurements were all taken at the same current, so no further normalization is necessary. 32
5.4 Experimental and simulated results for N-related defects in SiC. Figure from [8] . . 33
5.5 12,500 Hz modulated X band trace on SiC at $\theta = 0°$ with two hypothetical signals combined to recreate the experimental data. The cyan curve is a small, broad Gaussian, whereas the green curve is a Dysonian-like lineshape made from a Lorentzian and a Gaussian signal combined. Note that the green curve is not a Voight line, it is Lorentzian at values of B lower than the zero-crossing and Gaussian at B values higher than the zero-crossing. 34
5.6 Sideline spacing between sidelines in the 100 Hz traces and the zero-crossings of both the 100 Hz and 12,500 Hz centerlines. 36
5.7 Spacing between the hyperfine sidelines and a silicon vacancy, if it were present. . 37

Acknowledgements

I would like to thank Dr. Patrick Lenahan for his continued advice and support throughout this project. This work was also greatly assisted by James Ashton, whose numerous contributions to this project have also been incredibly valuable. I would also like to acknowledge my fellow graduate students in the Semiconductor Spectroscopy laboratory for their advice and support. Additionally, I would like to thank the United States Army Research Laboratory for their financial and general support of this project. The findings and conclusions of this work are not necessarily the views of this agency.

Twinkle twinkle little Spin
Are you single or are you twin?
Are you real or are you false?
How I crave your resonant pulse

A poem by John A. Weil, found in J. A. Weil and J. R. Bolton, *Electron paramagnetic resonance: elementary theory and practical applications*. Hoboken, N.J: Wiley-Interscience, 2nd ed., 2007.

Chapter 1

Introduction

Each and every day, the role of electronics in modern life becomes more prominent. From basic silicon devices in the postwar world to modern processors, low dimensional materials, and power electronics, new materials and methods have been investigated and applied to meet the needs of an ever-changing world. For high-power challenges, the latest material of choice is silicon carbide (SiC). Silicon carbide has potential for use in solar inverters, power supplies, and a myriad of other prominent roles less aptly met by conventional silicon [9].

Silicon carbide has a variety of properties that make it a valuable choice for high-power devices compared to traditional silicon. First, silicon carbide is a wide band gap semiconductor [9, 10]. The bandgap of the 4H-SiC polytype is 3.26 eV, about three times larger than that of silicon [9]. This property alone is valuable for mitigating some temperature-related electronic challenges. Silicon carbide also posses a higher melting point, breakdown field, and thermal conductivity than silicon [9]. This combination of traits has warranted extensive silicon carbide research and development. These developments are essential for meeting the modern demands for high power electronics.

One particularly useful high power device is a silicon carbide PIN diode. ”PIN” diodes are

named as such for the doping of the regions in the diode; PINs generally include a p-doped region, an ”intrinsic” region that is usually only lightly doped (about 10^{14} cm^{-3}), and an n-doped region. Devices made from silicon carbide with this structure sufficiently meet high-power and high-endurance needs.

Like the development of any material, a litany of technical challenges face researchers working with silicon carbide. SiC wafers are susceptible to basal plane dislocations and subsequently stacking faults [10]. Moreover, atomic defects, both intrinsically and from doping, can affect device performance in unforeseen and undesirable ways.

In order to meet the needs of modern consumers and of new technical challenges, the identification of performance limiting defects in silicon carbide is pertinent. This work seeks to identify and characterize those atomic defects within one type silicon carbide PIN diode. In doing so, it will help to elucidate the mechanisms by which many silicon carbide devices fail or do not match the desired performance.

Chapter 2

Literature Review

2.1 Electron Paramagnetic Resonance

Electron paramagentic resonance (EPR) spectroscopy is a technique that allows one to identify paramagnetic point defects in semiconductors and insulators [11]. Electrons have a quantized angular momentum, or ”spin,” of $\vec{S} = \pm\frac{1}{2}$. Moreover, this angular momentum contributes to a magnetic moment equal to $g\mu_\beta\vec{S}$, where g is the Landé factor for the electron and $\mu_\beta = 9.27 * 10^{-24}$ JT^{-1} is the Bohr magneton [11]. For an electron in a magnetic field, the energy difference between the two spin states increases linearly from their $B = 0$ positions with the magnetic field. This phenomena is called Zeeman splitting and can be described via

$$\Delta E = g\mu_\beta\vec{B} \cdot \vec{S}, \tag{2.1}$$

where ΔE is the difference in energy levels and B is the magnetic field [11]. We consider the magnetic field $\vec{B}$ to point in the z direction and equation 2.1 becomes

$$\Delta E = g\mu_\beta BS. \tag{2.2}$$

The difference between the energy levels of the $S = +\frac{1}{2}$ and $S = -\frac{1}{2}$ states is therefore twice this energy. An electron can be flipped from one spin state to the other by a photon with equivalent energy. The Planck-Einstein relationship tells us

$$E_{\text{photon}} = h\nu, \tag{2.3}$$

in which E_{photon} describes the energy of electromagnetic radiation, h is Planck's constant, and ν is the frequency of the photon [11]. In conventional EPR, combining eq. 2.2 for the total energy difference and eq. 2.3 lead to

$$h\nu = g\mu_\beta B. \tag{2.4}$$

In a real system, g is often dependent on the local environment. The g value or values that satisfy eq. 2.4 can sometimes determine a defect structure via EPR. Given that g is an unknown and that h and μ_β are constants, only B and ν are variables in eq. 2.4. Typically ν is held constant at a microwave frequency, and B is relatively slowly swept over a range of fields that satisfy eq. 2.4. While this occurs, the absorption of the constant photon source is measured. The field and frequency combination where resonance occurs are used to find a g value for the given defect. For reasons relating both to convenience and to phase-sensitive detection used to increase sensitivity, the derivative of absorption is often reported and used when discussing EPR lineshapes [11].

While often sufficient for a basic understanding of the typical resonance condition used in EPR spectroscopy, there are other physical parameters which can be added to equation 2.4 for greater analytic power. Electron-nuclear hyperfine interactions can often be detected [11]. Hyperfine lines generally are symmetric about the resonance condition corresponding to the values expected if no

nuclei were nearby, such that

$$B_{1,2} = \frac{h\nu}{g\mu_\beta} \pm \frac{A}{2} g\mu_B. \tag{2.5}$$

Here A is called the hyperfine coupling. It is often expressed as a second rank tensor.

$$A = \frac{2\mu_0}{3} g\mu_B\mu_N \mid \psi(0) \mid^2, \tag{2.6}$$

where μ_N is the nuclear magneton and ψ is the wave function [12]. If the hyperfine interactions are due to distant nuclei, the interactions are often of the Fermi-contact form as described be expression 2.6.

Suppose a system has $S = \pm\frac{1}{2}$ and nuclear spin $I = \pm\frac{1}{2}$. There are therefore four total states an electron could occupy such that two transitions can be detected [11]. These two additional peaks are the hyperfine peaks that occur on, in general, either side of the centerline. The spacing and relative integrated intensities of the hyperfine sidelines can generally be linked back to parameters in magnetic nuclei. Knowing which atoms influence a signal via the hyperfine parameters affords EPR even greater spectroscopic power.

Many spectra appear with two equally spaced hyperfine peaks when $\mid I \mid = \frac{1}{2}$, but more lines can appear when $\mid I \mid > \frac{1}{2}$. In general, there are $2I + 1$ lines [11]. For example, nitrogen has $I = 1$ and therefore has a three-line spectrum [2]. The magnitude of this signal to the centerline is dependent upon the relative abundance of different isotopes. ^{14}N has near 100% abundance, so the three-line spectrum is expected to have three equal peaks [2]. For silicon, ^{28}Si has $I = 0$. However, ^{29}Si has $I = \frac{1}{2}$ and a relative abundance of about 4.7%, so the spectrum should feature a strong centerline with two side peaks with a combined integrated intensity of about 4.7% [7].

2.2 Electrically Detected Magnetic Resonance

Conventional EPR is useful for studying bulk materials, but it is sometimes insufficient for studying modern semiconductor devices because the total number of defects in a given device is

often lower than the sensitivity of EPR [2]. Conventional EPR has a sensitivity of about 10^{10} total defects [2]. This means that the number of defects in a modern electronic device may be altogether too small for detection via conventional EPR. A closely-related technique that can be used with great efficacy on these devices is electrically detected magnetic resonance (EDMR) spectroscopy.

In contrast to EPR, where defect detection is based on photon absorption, dispersion, or reflection, EDMR is based on detecting changes in current [13]. While EPR processes are often dependent upon spin polarization, EDMR is granted additional sensitivity because this is not always a requirement for EDMR detection [13]. As a results, continuous wave EDMR has about 10^7 times more sensitivity than conventional EPR [14].

A variety of different spin-dependent mechanisms have been detected via EDMR. Two of the most common are spin dependent trap assisted tunneling (SDTAT) and spin dependent recombination (SDR). In SDTAT, electrons tunnel from trap to trap, generally in an oxide, in a manner akin to variable range hopping [1]. An illustration of this is included in figure 2.1. SDTAT has been used with a great deal of efficacy in detecting defects in insulating materials like a-SiC [1].

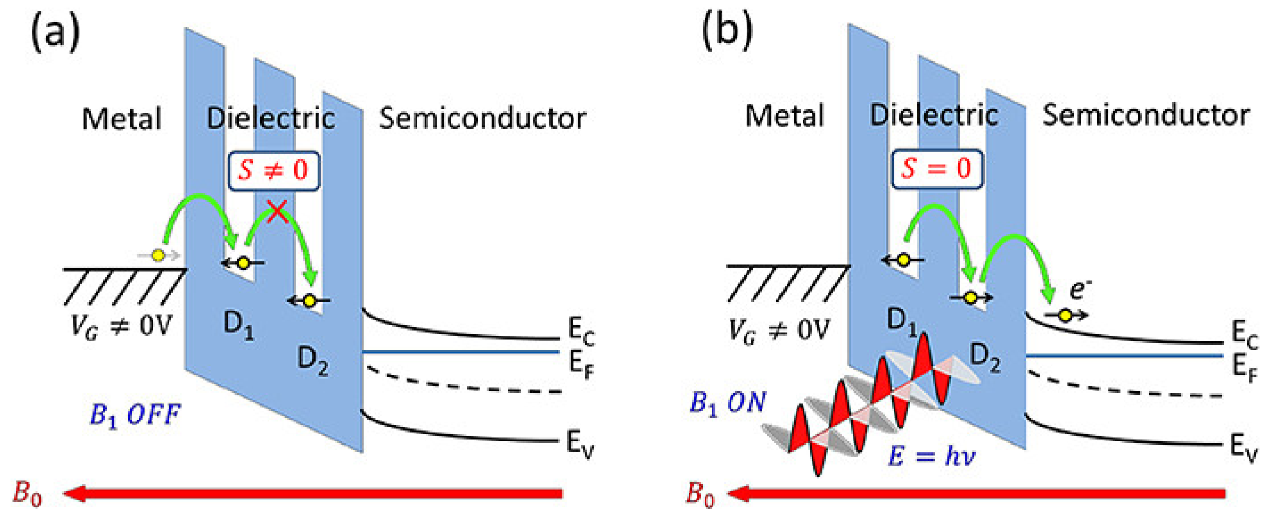

Figure 2.1: A simple illustration of spin dependent trap assisted tunneling. D1 and D2 represent trap locations, B1 is the quasistatic magnetic field, and the diagram otherwise uses conventional band diagram notation. In a), the tunneling event is forbidden, whereas in b) it is allowed because the charge carrier spin has been flipped at the resonance condition. Figure from [1].

The most popular EDMR mechanism in literature is SDR [2, 15, 16, 17]. SDR can be understood in terms of the Shockley-Read-Hall model, the Pauli exclusion principle, and magnetic

resonance phenomena to allow for relatively precise defect detection [15, 17]. A typical SDR event may include a conduction electron and an electron at a defect, like a dangling bond. If the spins of the charge carrier and the deep level center are the same, the conduction electron cannot move into the defect. However, if the spin in the deep level defect is flipped, it can fill the defect site as its occupation of the orbital would no longer violate the Pauli exclusion principle. A hole could therefore recombine with the trapped electron and increase the overall recombination rate. Hence, SDR modifies the recombination current through the manipulation of the electron spin [14]. Note the electron-hole process does not need to occur in this order [17].

While conventional commercial EPR equipment is often a nontrivial portion of a standard EDMR setup, additional equipment is required. Biasing equipment is needed to generate a current in the studied device. Equipment to measure and record the current across the device is also needed. Most EDMR spectrometers use lock-in amplifiers, which are sometimes implemented digitally.

EDMR's detection requirements also enable measurements to be implemented over a wide range of frequencies. For example, one could compare the EDMR spectrum for a sample under $\nu = 9.5$ GHz to that of the same sample under $\nu = 0.5$ GHz. In addition to gleaning information from changes in the lineshape of the centerline, equation 2.5 suggests that the hyperfine spacing from the centerline should be independent of ν. In this way, the presence of hyperfine features can be distinguished from nearby linshapes for potentially unrelated defects by comparing data at two different frequencies more easily in EDMR [14].

2.3 Electron Paramagentic Resonance Results in SiC Devices

EPR techniques have been used on SiC devices with varying levels of effectiveness. A large portion of the published literature focuses on defect detection in MOSFETs, typically via EDMR [15, 18, 19, 20]. Additionally, EDMR has also been used to study PN diodes [2, 21]. No work using EPR techniques on SiC PIN diodes is readily available in the literature. The current work is therefore novel and will need to use closely related devices, namely conventional PN diodes and

MOSFETs, for comparison. The review of these works will largely focus on devices with similar dopants to the PINs investigated in this work.

Many SiC devices are doped with nitrogen [2, 22]. In diodes, nitrogen replaces carbon and acts as a shallow donor [2]. MOSFETs are often treated with NO and then annealed [2]. The NO anneals substantially impact transistor performance. Doping SiC is difficult because diffusing dopants thermally requires very high temperatures [22]. SiC crystals are often doped via ion implantation and then annealed at temperatures as high as 1700°C [2, 22].

Many studies have attempted to identify and characterize nitrogen and nitrogen-related defects in SiC [2, 23]. Work using electron spin echo (ESE) EPR and electron nuclear double resonance (ENDOR) have demonstrated that isolated N_C(k) and N_C(h) sites, the quasi-cubic and hexagonal sites, respectively, are both $S = \frac{1}{2}$ systems [23]. An additional defect, labeled the "N_x" defect, includes factors from both the N_C(k) and N_C(h) defects and has been associated via ESE with a $S = 1$ system [23].

Diodes with nitrogen doping sometimes introduces dominating nitrogen-related defects [2]. In a comparison of defects between samples with nitrogen implantation versus n+ region development via epitaxial growth, the N-implanted sample featured a signal intensity of over 100 times the epitaxially grown sample [2]. Moreover, the implanted sample featured a three-line spectra with equal integrated intensities of about 27%, a feature typical of defects with $I = 1$ like nitrogen [2, 11]. These results are depicted in figure 2.2.

The spectra depicted in figure 2.2 is when B is parallel to the crystalline-c axis for two different SiC PN diodes [2]. While $g_{\parallel} = 2.0048$ in figure 2.2a, $g_{\perp} = 2.0005$ in the same device [2]. Thus, nitrogen and nitrogen-related defects have a tendency to show some level of g anisotropy. Conversely, the results in figure 2.2b suggest an intrinsic defect like a silicon vacancy, often denoted V_{Si}, which has about $g = 2.003$ and is isotropic [20, 21].

Aichinger et al. eliminate a variety of defects as potential candidates in their device. First, they eliminated isolated substitutional nitrogen because such a defect would be too shallow to appear in SDR; the technique is sensitive only to deep-level defects [2, 24]. Moreover, the spectrum in figure

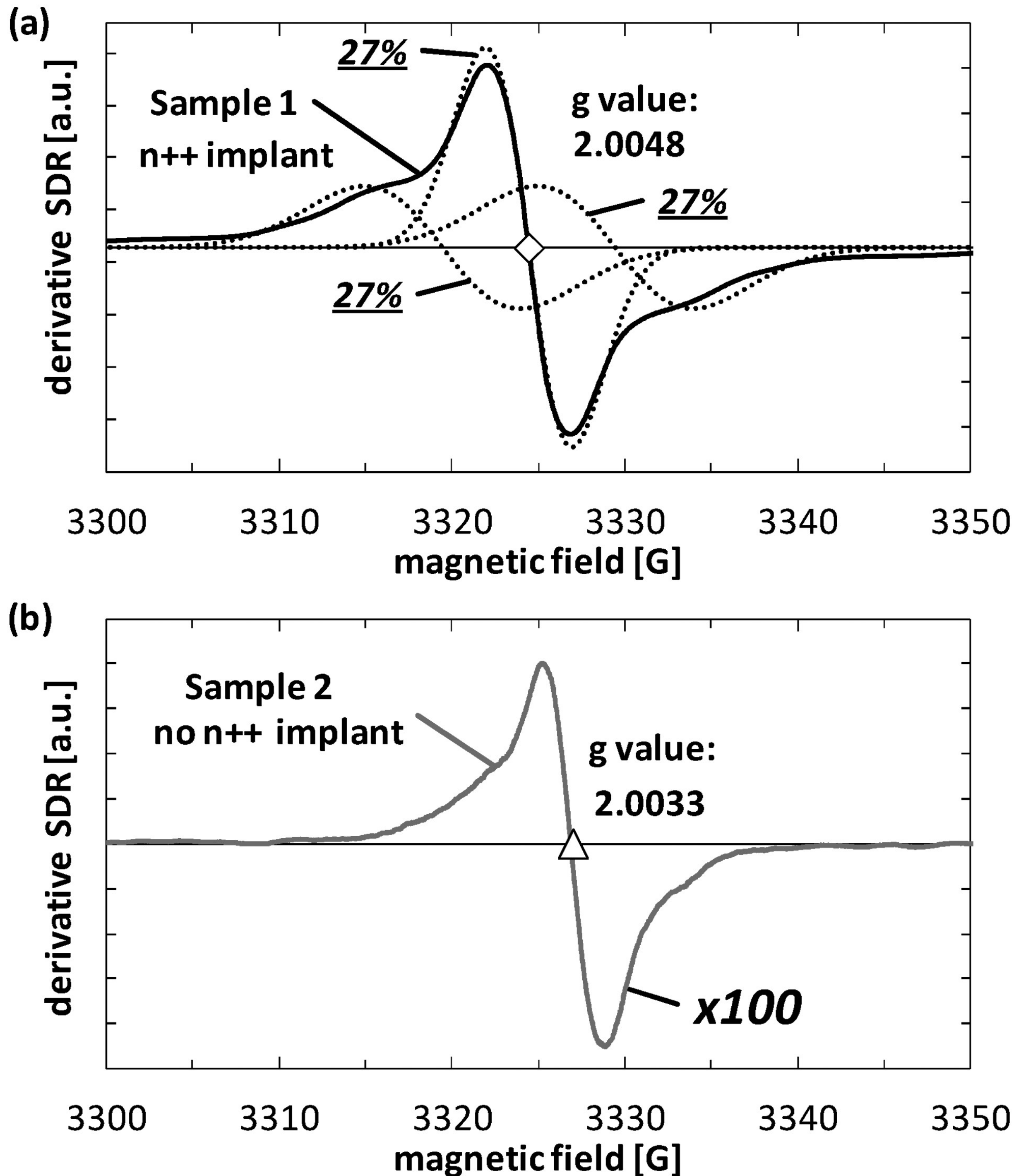

Figure 2.2: EDMR results on PN diodes that a) have n++ implantation and b) do not have n++ implantation. Figure from [2].

2.2a is different from a reported substitutional nitrogen spectrum, which has been previously captured via ESE and is depicted in figure 2.3. Second, the defect could not be the N_x defect because

the N_x defect is not reported to be easily detectable above 70 K and because it is too shallow for detection via SDR [2, 4]. The authors ultimately suggest that "[t]he dominating three-line character of the spectrum and the additional HF interactions suggest a deep-level defect complex which involves one nitrogen atom and an additional "intrinsic" defect structure. Candidates for the defect complex are a nitrogen coupled to a vacancy, an antisite, or a vacancy-antisite pair [2]."

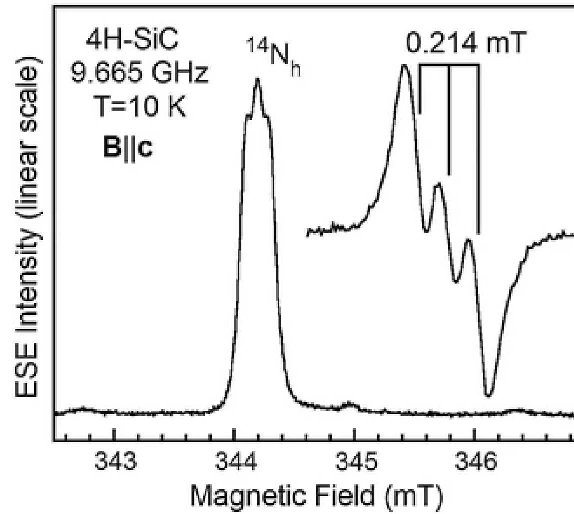

Figure 2.3: ESE results for subtitional nitrogen in 4H-SiC. While not explicitly reported, the centerline has about $g = 2.006$. Figure from [3].

The N_x defect is detected in heavily doped SiC via EPR and appears as the combination of one Lorentzian lineshape and one Dysonian lineshape [4]. The Dysonian lineshape is observed often in near-conductive semiconductors like n-type SiC [4]. Two $S = \frac{1}{2}$ spin systems were defined: one with a Dysonian lineshape that was associated with conduction electrons and the other with a Lorentzian lineshape that was associated with local donor electrons [4]. These results are depicted in figure 2.4. A range of g from $g_{\parallel} = 2.0045$ to $g_{\perp} = 2.0003$ are reported for the overall Dysonian lineshape [4].

One factor that varies between the detection of the N_x defect and other nitrogen or nitrogen-related defects is the dependence on temperature. The N_x defect is reported as having a greater signal-to-noise ratio at low temperatures like 15 K [4]. However, the signal becomes dramatically broader and diminished at higher temperatures. The authors suggest that the temperature dependence realized is described by a combination of temperature dependent paramagnetic phenomena

like Curie-Wiess and Pauli paramagnetism [4]. The lineshape depicted in figure 2.2a is marked as being different from that in figure 2.4 not only by a difference in lineshape, but also because the data in figure 2.2a is taken at 300 K. The N_x defect as detected by Savchenko et al. is difficult to detect at higher temperatures, ruling out the possibility of overlap between the N_x defect and the nitrogen-intrinsic defect complex detected by Aichinger et al. [2, 4].

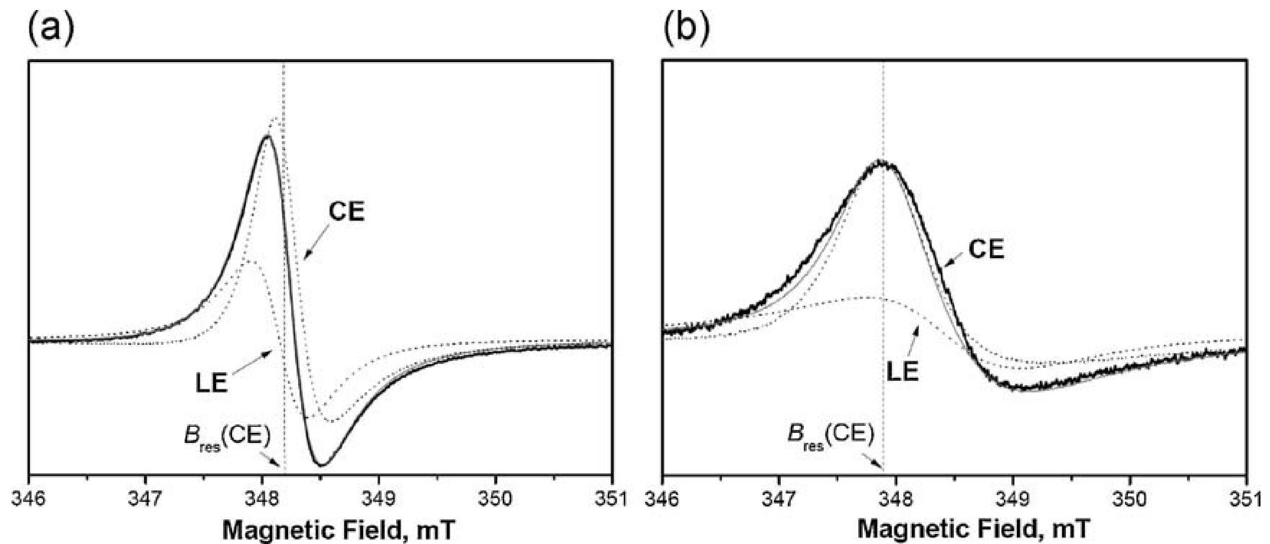

Figure 2.4: $N_x$defect in heavily doped n-type 4H SiC at a) 15K and b) at 70 K. Figure from [4].

Work on SiC n+p diodes with both N-implants and P-implants report spectra with isotropic gs of 2.0029 [21]. Both feature slightly anisotropic hyperfine side peaks, with 10.4 G separation for C $\perp$ B_0 and 13 G separation for C $\parallel$ B_0 [21]. The dominant SDR defect in this case has results which are consistent with a silicon vacancy [21]. Here, however, the N-implanted defects have a much broader signal, especially when perpendicular to the crystalline-c axis. This is attributed to higher disorder around defects [21]. This work also used a modulation magnitude of about 1 G, and the overall peak-to-peak width of the centerlines is less than 10 G in all X-band cases. The N-implanted signal features greater broadening as a result of rotation than the P-implanted device [21].

Applying previous results on PN diodes to PIN diodes is a relatively straightforward comparison given that the only major difference is the presence of an intrinsic region in the PIN diodes. Comparing EPR results in MOSFETs to diodes is slightly less direct because many of the defects

detected in MOSFETs are detected using techniques like spin dependent charge pumping (SDCP), which are inherently more sensitive to defects located at the interface of the oxide [15].

However, some SDCP schemes have included parameters which suggest that defects inherent to the depletion region were detected, rather than interface defects [15]. Anders et al. detect silicon vacancies via SDCP while holding the gate at extremely high positive voltage. This holds the MOSFET in inverison, effectively dominating the channel with only one type of charge carrier [15]. Despite this, a recombination-driven signal is still detected, suggesting that some dominating defects are intrinsic to SiC and found in the region below the SiC/SiO_2 interface [15]. This suggests that literature reporting defects at the interface of SiC MOSFETs may still be applicable to devices without an oxide layer insofar as it is relevant for near-surface defects.

While the device schematic is presented in the next section, it is also worth noting that real diodes do not exist in a realm devoid of real encasing and enclosures. An oxide layer often envelops electrical devices to protect it from the outside environment [6]. Oxide-SiC interface defects should also be considered as possible defect sources given that edge-located defects could be sources of additional carrier contributions or traps. Considering defects in this region should be relatively comparable to defect identification at the oxide-SiC interface in SiC MOSFETs even without needing to consider the applicability of near-interface defects within the semiconducting material as mentioned by Anders et al.

Chapter 3

Methods

EDMR measurements were taken on a SiC PIN diode at angles ranging from $\theta = 0°$ to $\theta = 165°$ in increments of $15°$, where θ is the angle between the direction normal to the device face and the quasistatic magnetic field. g values for each of these angles were calculated. All measurements were taken at X-band, with approximately $\nu = 9.6$ GHz. Individual device angles caused the cavity to tune to different frequencies, so data is normalized to $\nu = 9.6$ GHz when necessary. A 3 G modulation was applied. Two different modulation frequencies were used: 12,500 Hz and 100 Hz, a "high modulation" set and a "low modulation" set, respectively. Preliminary testing suggests that results are similar for modulation frequencies above about 1,000 Hz and for frequencies where relatively clear measurements are achievable below about 1,000 Hz. Thus, the modulation frequencies were selected on the basis that they are far enough apart to see differences in the results and because they each allow for an acceptable signal-to-noise ratio. The diodes were current matched to 1.5 μA at each angle.

Measurements were taken on a homemade spectrometer which uses a Lakeshore electromagnet, a Lakeshore power supply, and homemade data acquisition software. The modulation frequen-

cies were matched via a digital lock-in amplifier to improve the signal-to-noise ratio. Data analysis was done using MATLAB 2019b. Figure 3.1 illustrates most of the EDMR spectrometer system. Note that the electromagnet schematic in the figure does not include all of the components featured on the setup used in this work.

Also note that the experimental design for this project includes some practical limitations imposed by the pandemic ongoing at the time of writing. A more rigorous experiment, and the intended experiment in many ways, would more thoroughly display the frequency dependence of the results. Moreover, the device would be rotated about more than one axis. Unfortunately, this was not possible within the time limits imposed on this project.

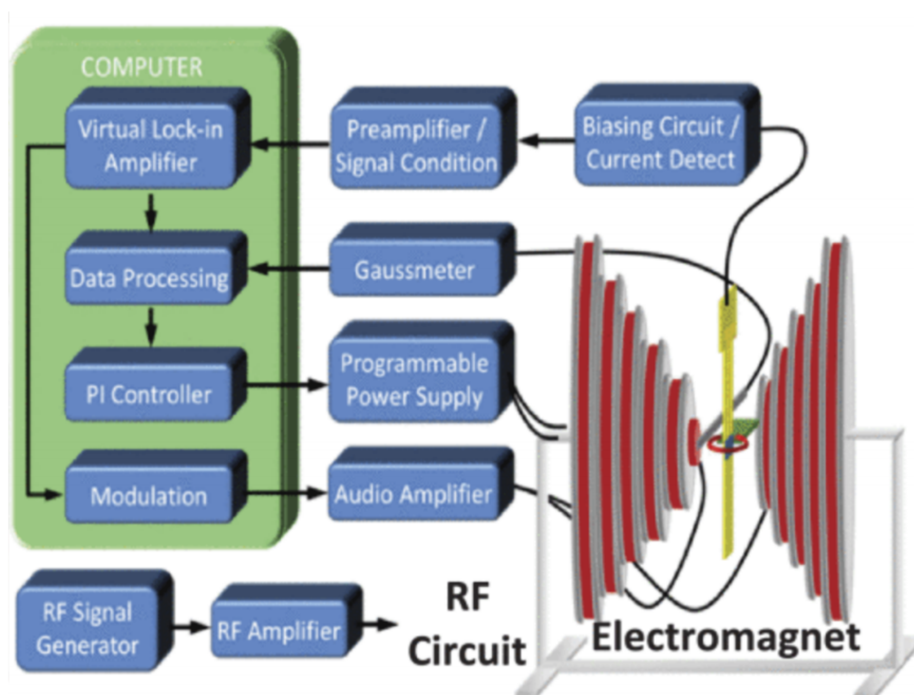

Figure 3.1: Schematic of an EDMR spectrometer. Note that the electromagnet schematic in the figure does not include all of the components featured on the spectrometer used in this work. Figure from [5].

The PIN device used is similar to those reported by Hull et al [6]. The layout is depicted in figure 3.2. The PIN is doped with Al as a p-type dopant and N as an n-type dopant. A feature called the junction termination extension (JTE) is also included as a means of improving device performance.

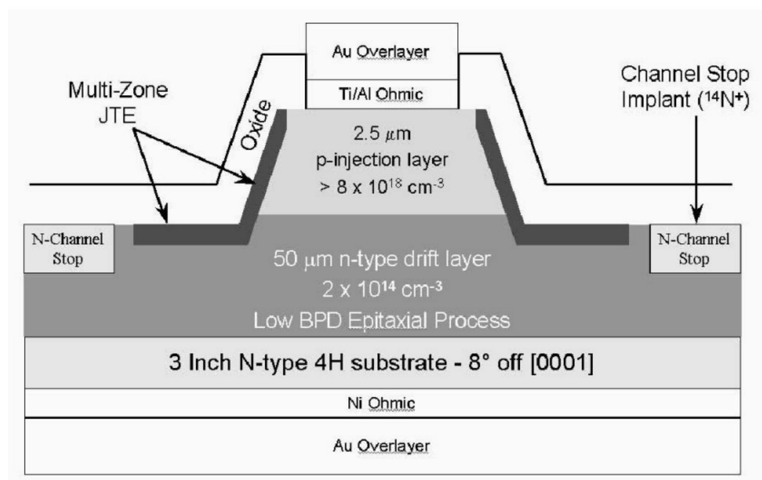

Fig. 2. Schematic cross-section of 4.5 kV 4H-SiC PiN diode.

Figure 3.2: Schematic for the SiC PIN diode most similar to that used in this work. Note that the exact dimensions of the PIN used in this work are not necessarily the same or similar to this figure. The figure should only be used to have an understanding of what the PIN is like. Figure from [6].

Chapter 4

Results

Figures 4.1 – 4.24 illustrate signal-averaged EDMR traces for the SiC PIN diode. All figures are normalized to $\nu = 9.6$ GHz. The figures are organized by angle of rotation, where the red traces are high modulation frequency results and the blue traces are low modulation frequency results. The angle described is the difference between the direction normal to the face of the device and the magnetic field. In other words, $\theta = 0^\circ$ refers to the direction where the device-normal direction is parallel to the quasistatic magnetic field, whereas $\theta = 90^\circ$ is perpendicular when the device is rotated about one axis. Limitations imposed by the pandemic limited this experiment to only one axis of rotation and limited our ability to gain $\theta = 180^\circ$ results, but a more rigorous experiment would include rotations about three directions and the final points.

4.1 $\theta = 0°$

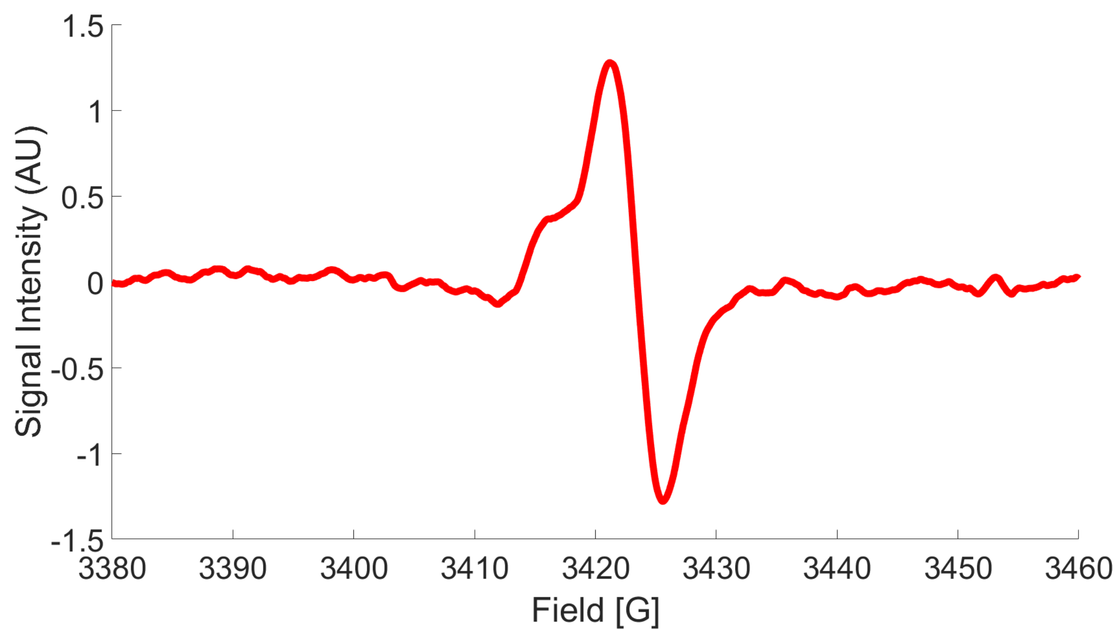

Figure 4.1: Data at $\theta = 0°$ and a modulation frequency of 12,500 Hz.

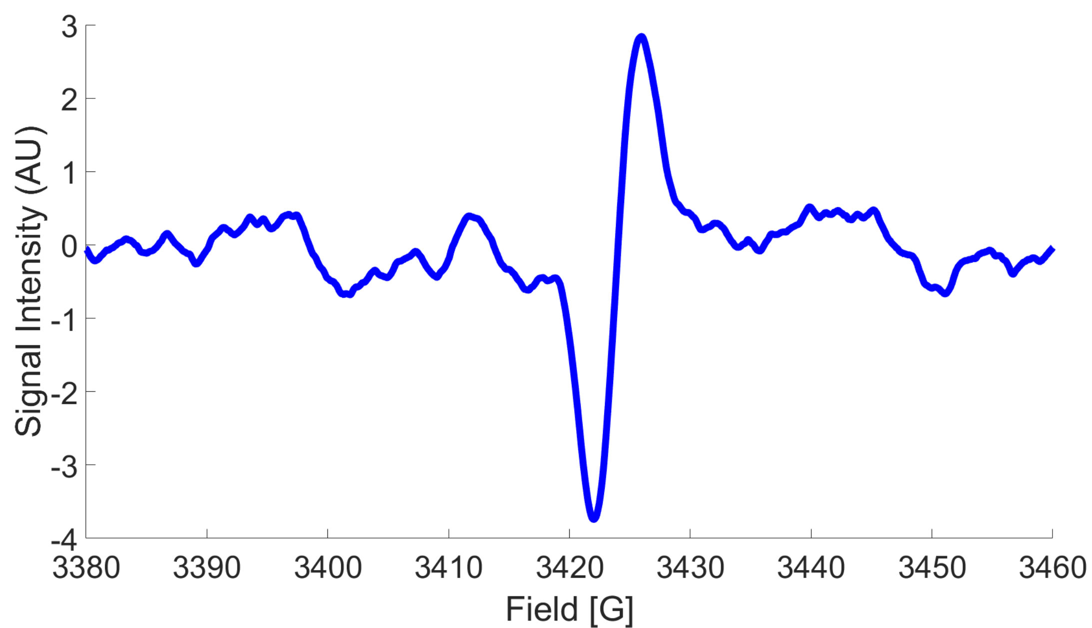

Figure 4.2: Data at $\theta = 0°$ and a modulation frequency of 100 Hz.

4.2 $\theta = 15°$

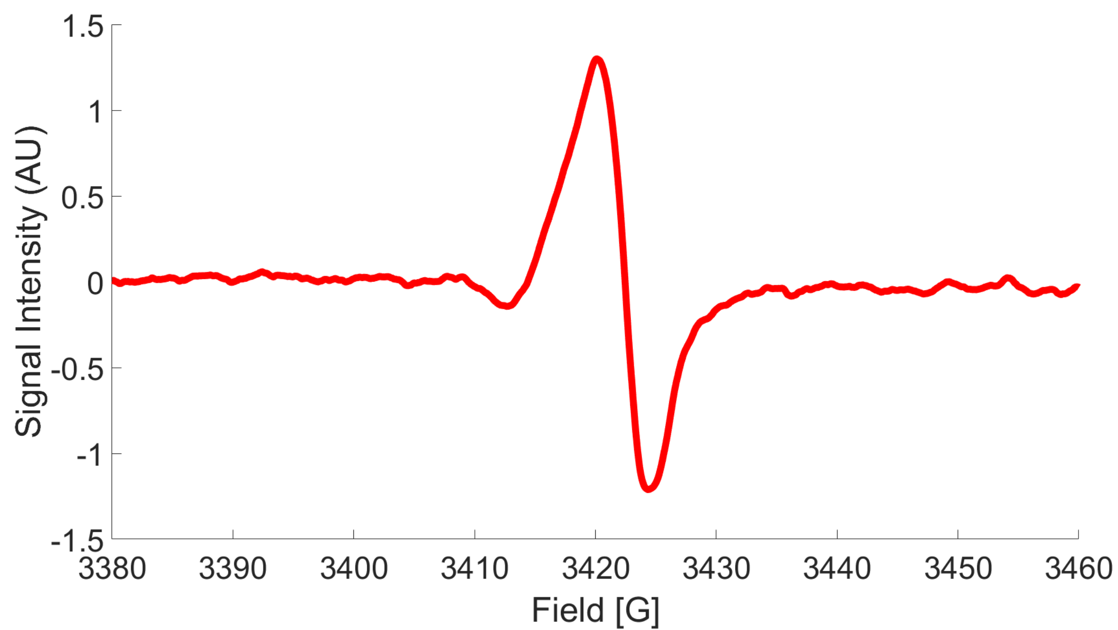

Figure 4.3: Data at $\theta = 15°$ and a modulation frequency of 12,500 Hz.

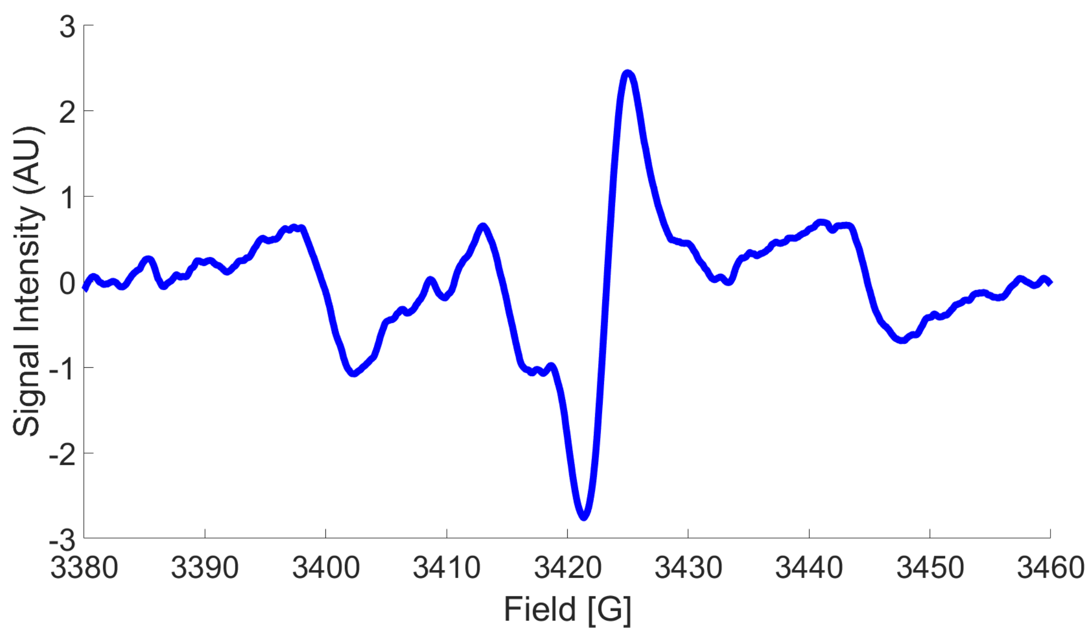

Figure 4.4: Data at $\theta = 15°$ and a modulation frequency of 100 Hz.

4.3 $\theta = 30^\circ$

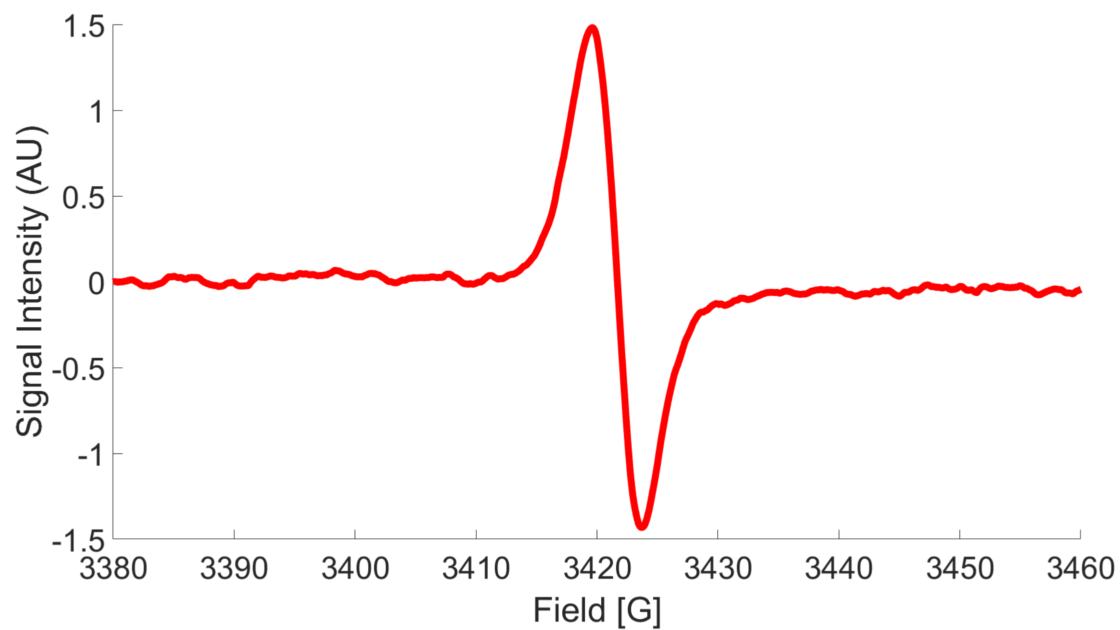

Figure 4.5: Data at $\theta = 30^\circ$ and a modulation frequency of 12,500 Hz.

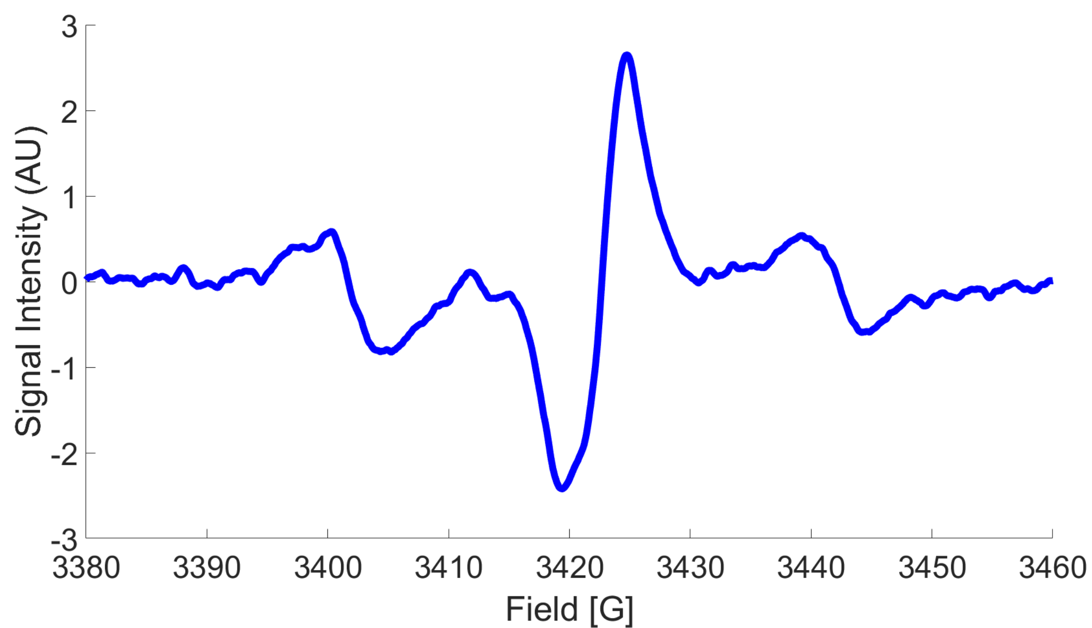

Figure 4.6: Data at $\theta = 30^\circ$ and a modulation frequency of 100 Hz.

4.4 $\theta = 45^\circ$

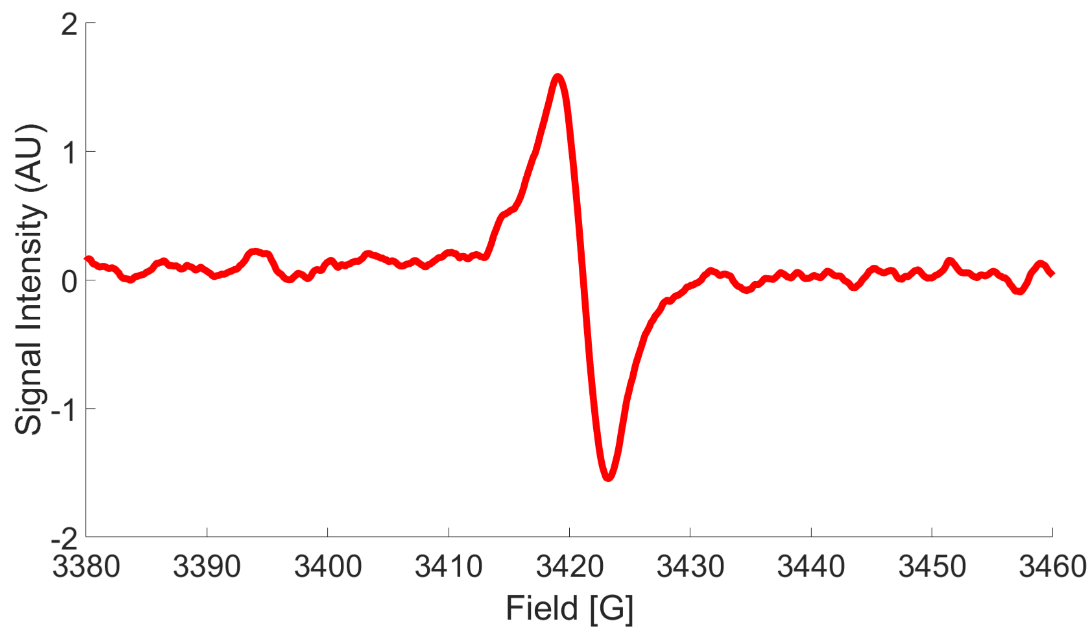

Figure 4.7: Data at $\theta = 45^\circ$ and a modulation frequency of 12,500 Hz.

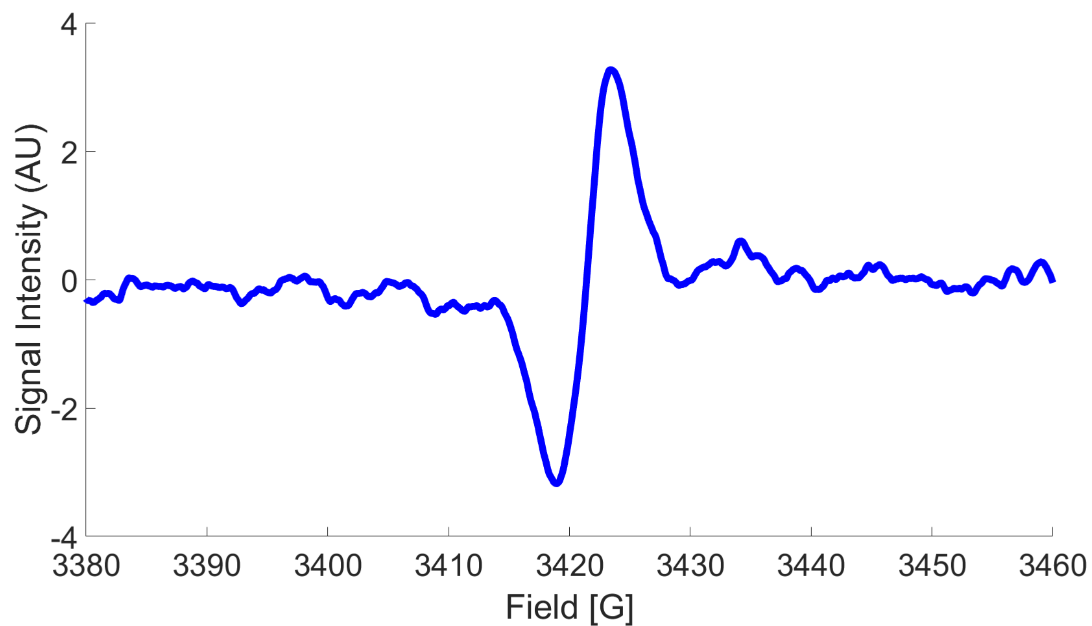

Figure 4.8: Data at $\theta = 45^\circ$ and a modulation frequency of 100 Hz.

4.5 $\theta = 60^\circ$

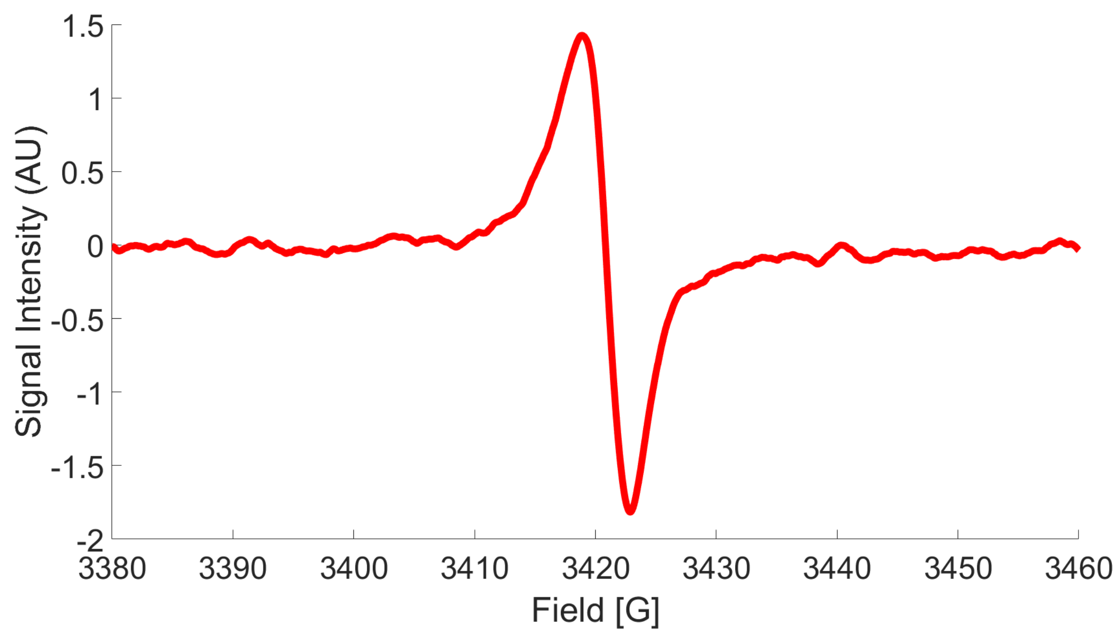

Figure 4.9: Data at $\theta = 60^\circ$ and a modulation frequency of 12,500 Hz.

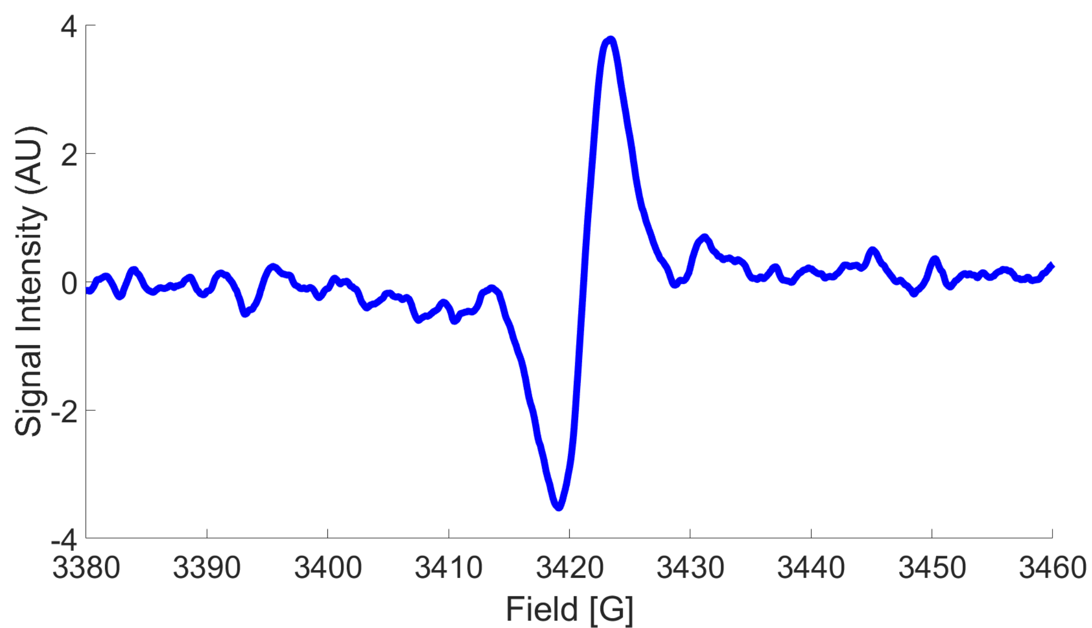

Figure 4.10: Data at $\theta = 60^\circ$ and a modulation frequency of 100 Hz.

4.6 $\theta = 75°$

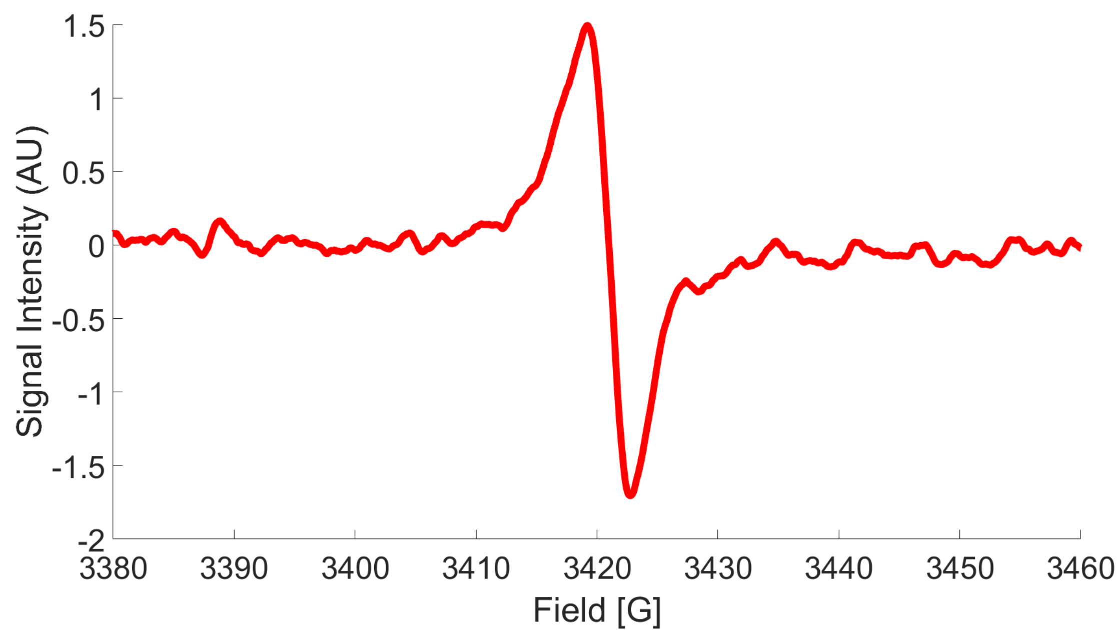

Figure 4.11: Data at $\theta = 75°$ and a modulation frequency of 12,500 Hz.

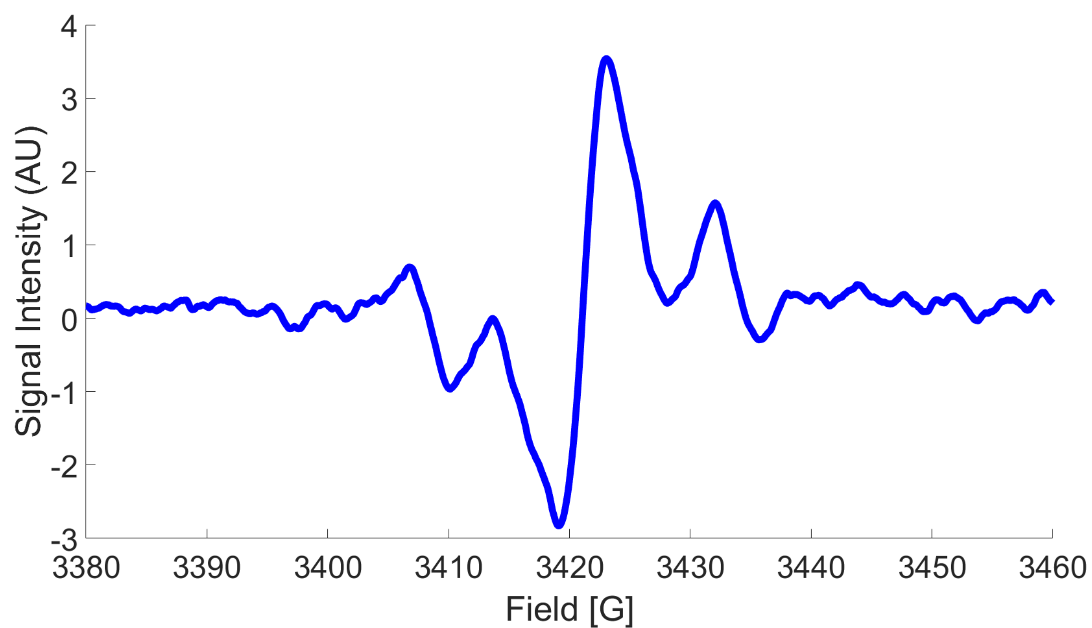

Figure 4.12: Data at $\theta = 75°$ and a modulation frequency of 100 Hz.

4.7 $\theta = 90°$

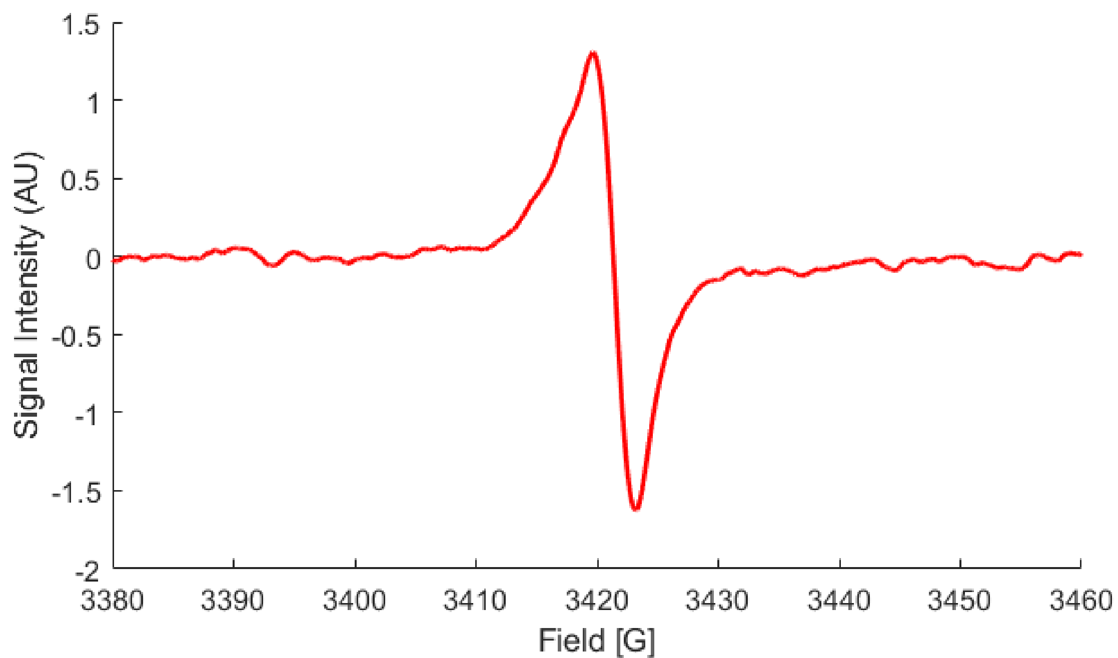

Figure 4.13: Data at $\theta = 90°$ and a modulation frequency of 12,500 Hz.

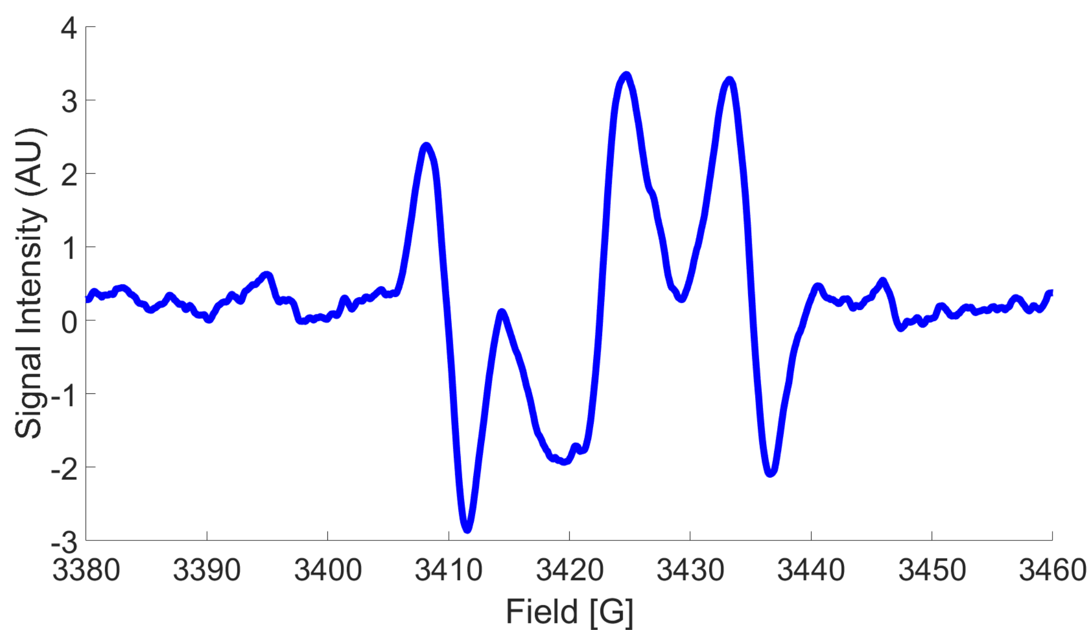

Figure 4.14: Data at $\theta = 90°$ and a modulation frequency of 100 Hz.

4.8 $\theta = 105^\circ$

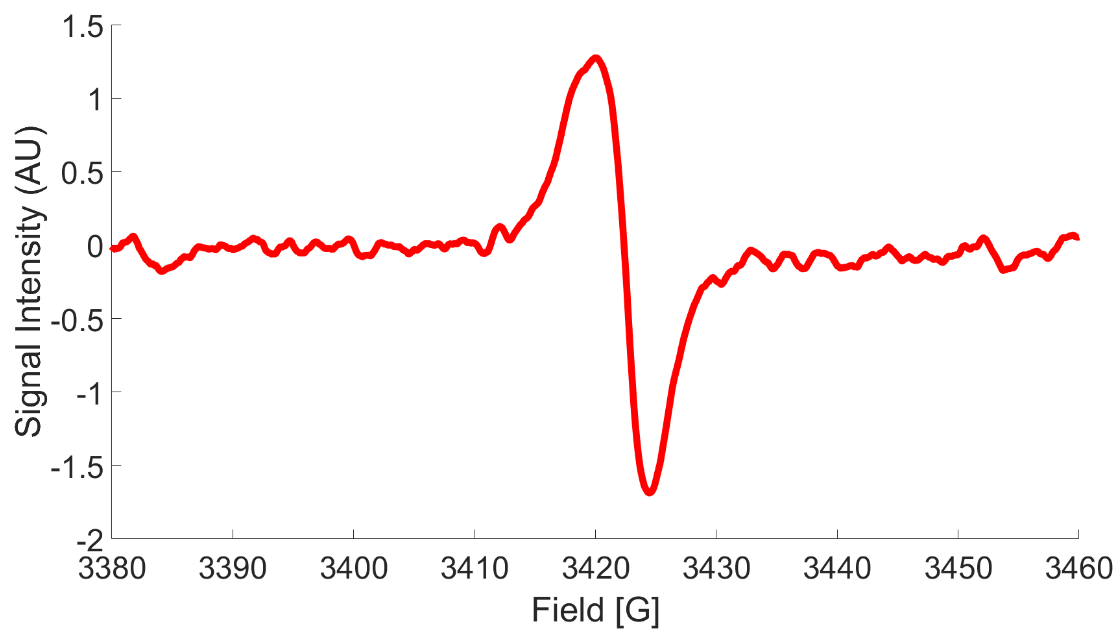

Figure 4.15: Data at $\theta = 105^\circ$ and a modulation frequency of 12,500 Hz.

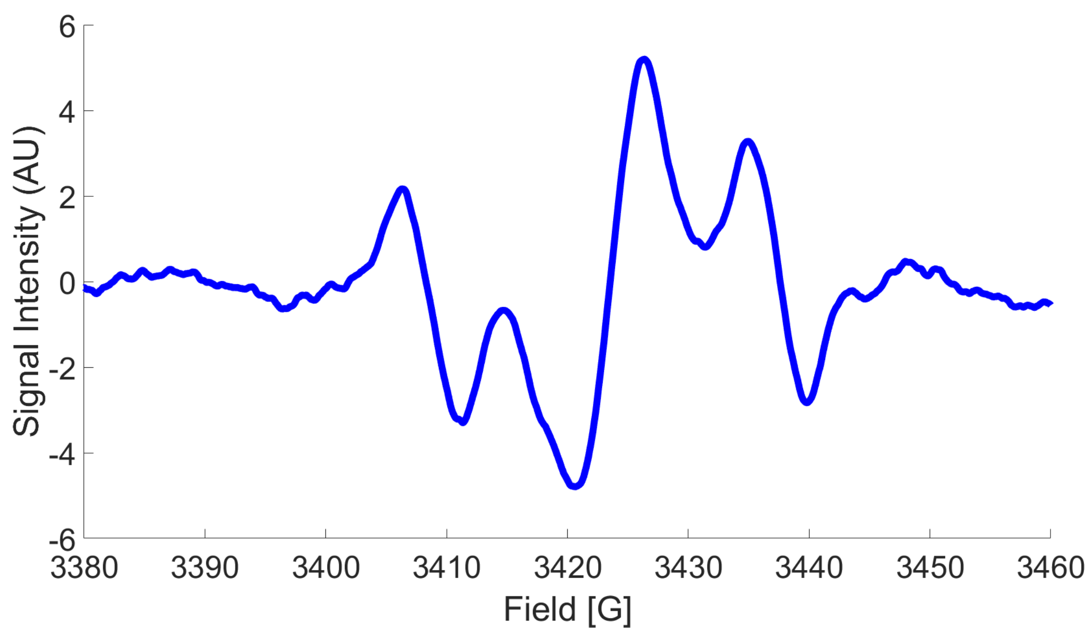

Figure 4.16: Data at $\theta = 105^\circ$ and a modulation frequency of 100 Hz.

4.9 $\theta = 120°$

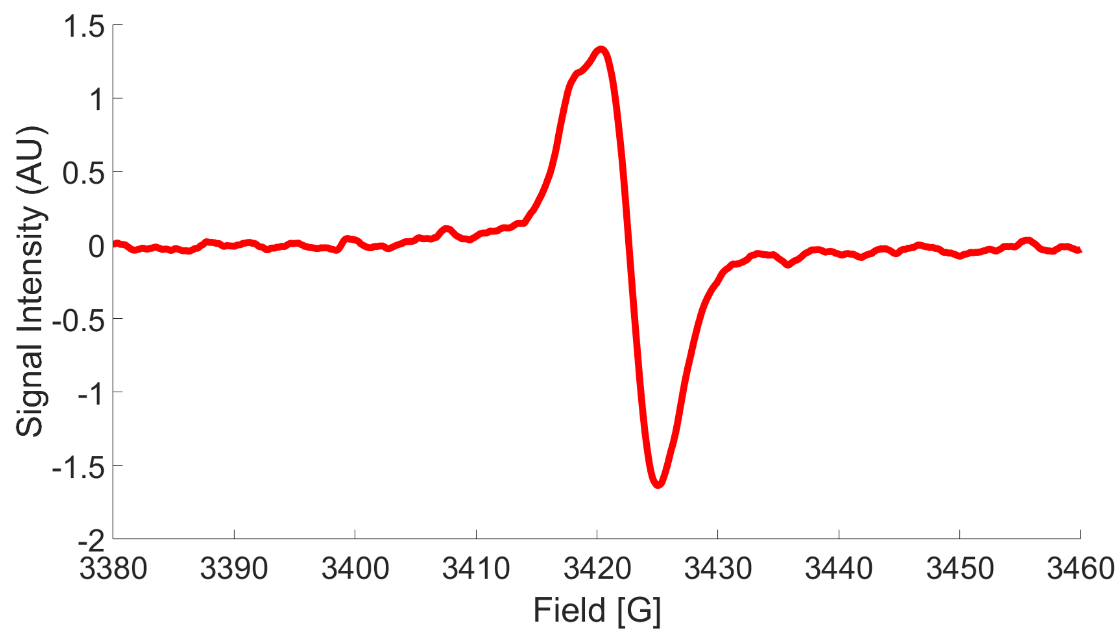

Figure 4.17: Data at $\theta = 120°$ and a modulation frequency of 12,500 Hz.

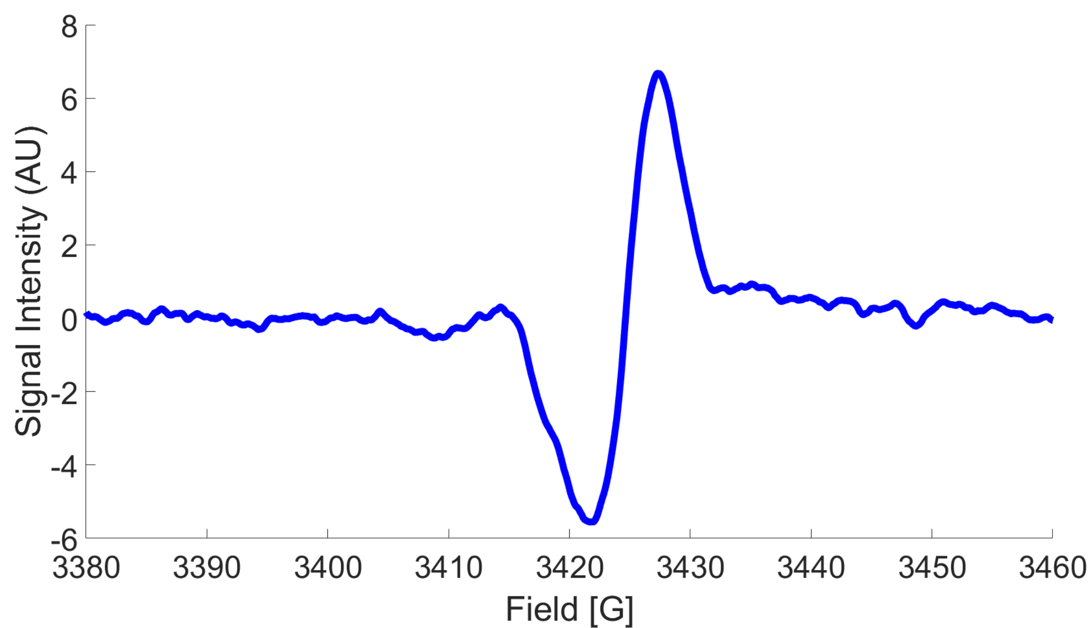

Figure 4.18: Data at $\theta = 120°$ and a modulation frequency of 100 Hz.

4.10 $\theta = 135°$

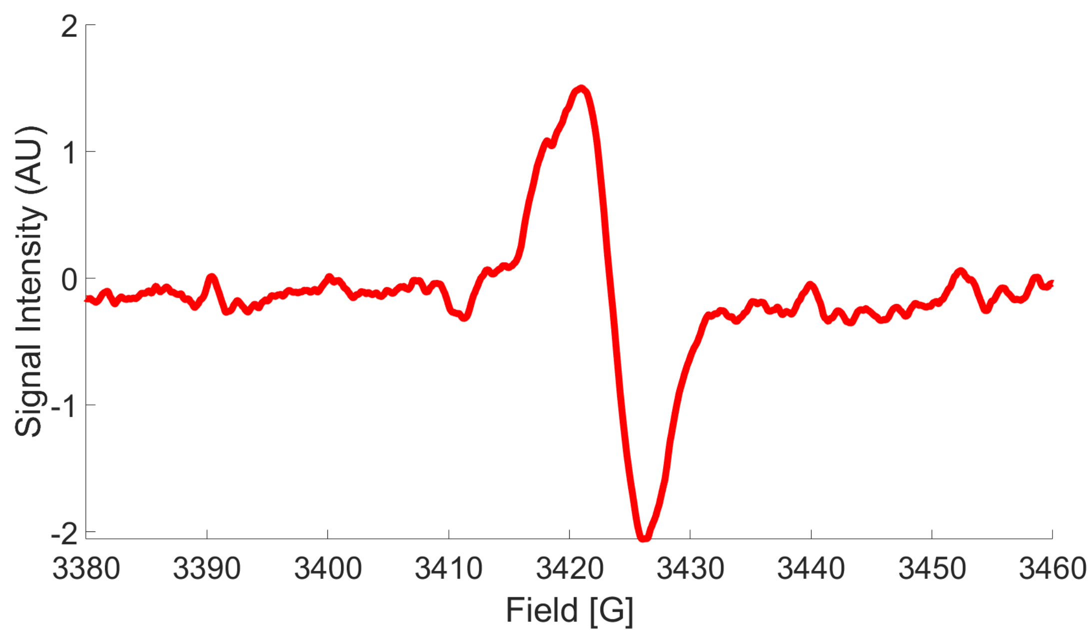

Figure 4.19: Data at $\theta = 135°$ and a modulation frequency of 12,500 Hz.

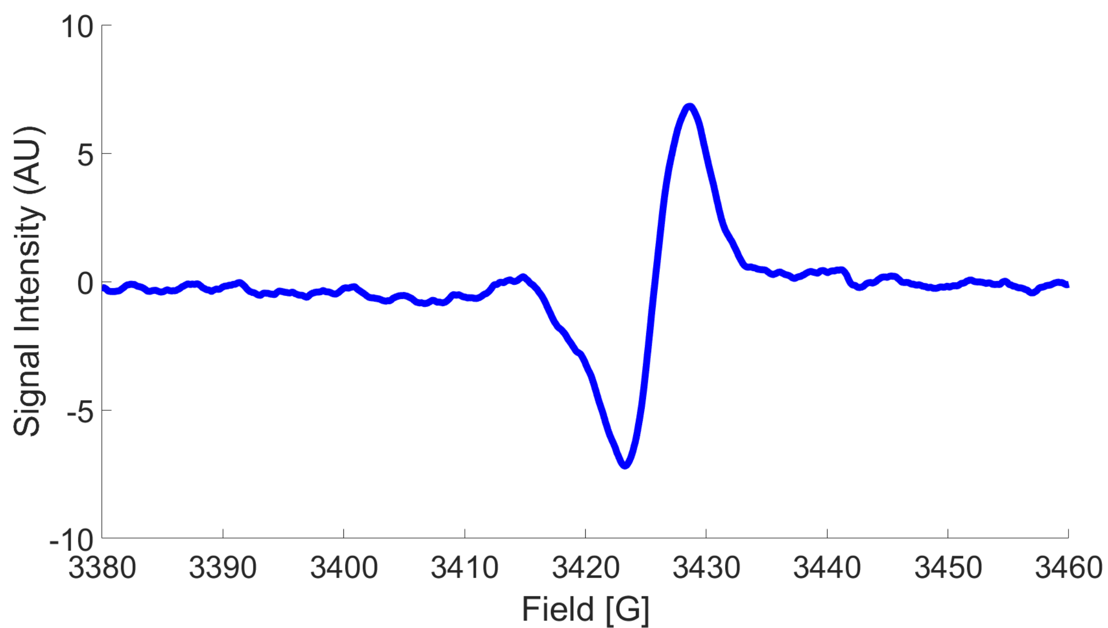

Figure 4.20: Data at $\theta = 135°$ and a modulation frequency of 100 Hz.

4.11 $\theta = 150^\circ$

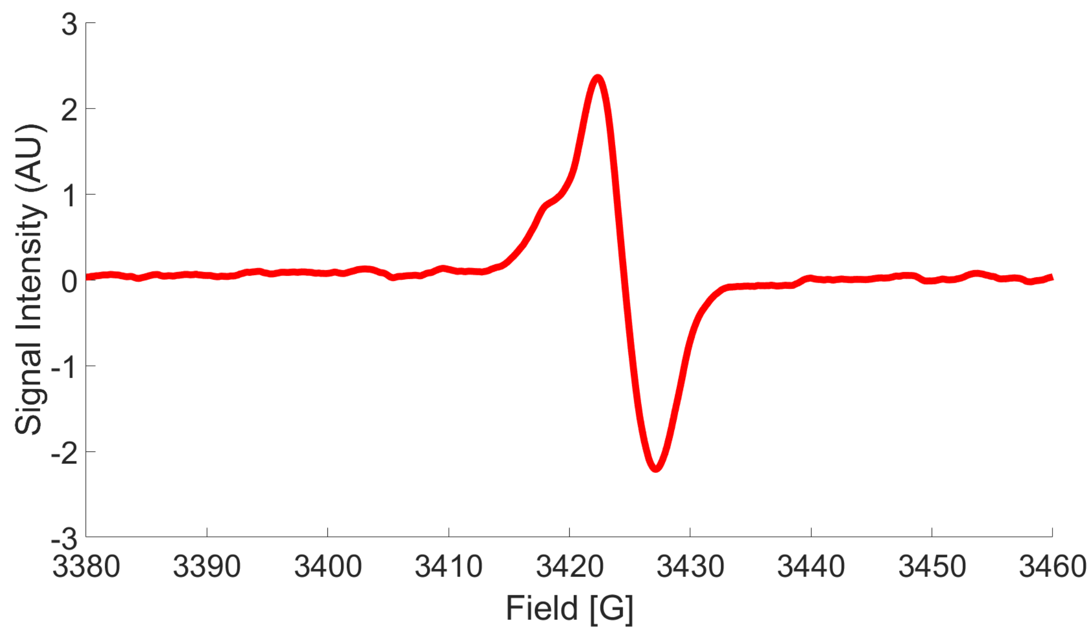

Figure 4.21: Data at $\theta = 150^\circ$ and a modulation frequency of 12,500 Hz.

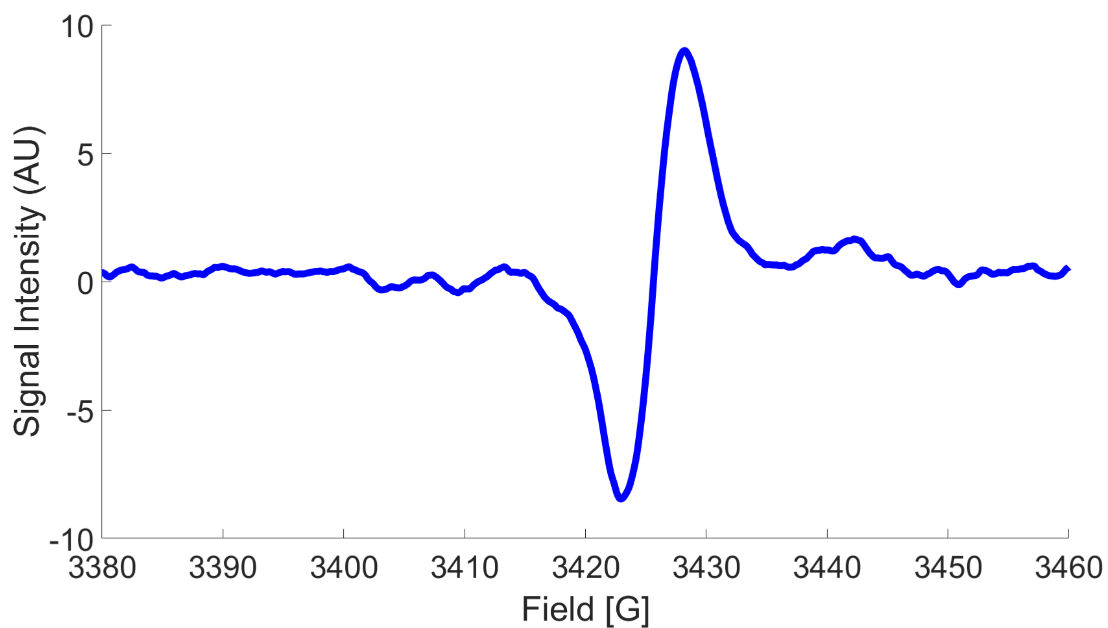

Figure 4.22: Data at $\theta = 150^\circ$ and a modulation frequency of 100 Hz.

4.12 $\theta = 165°$

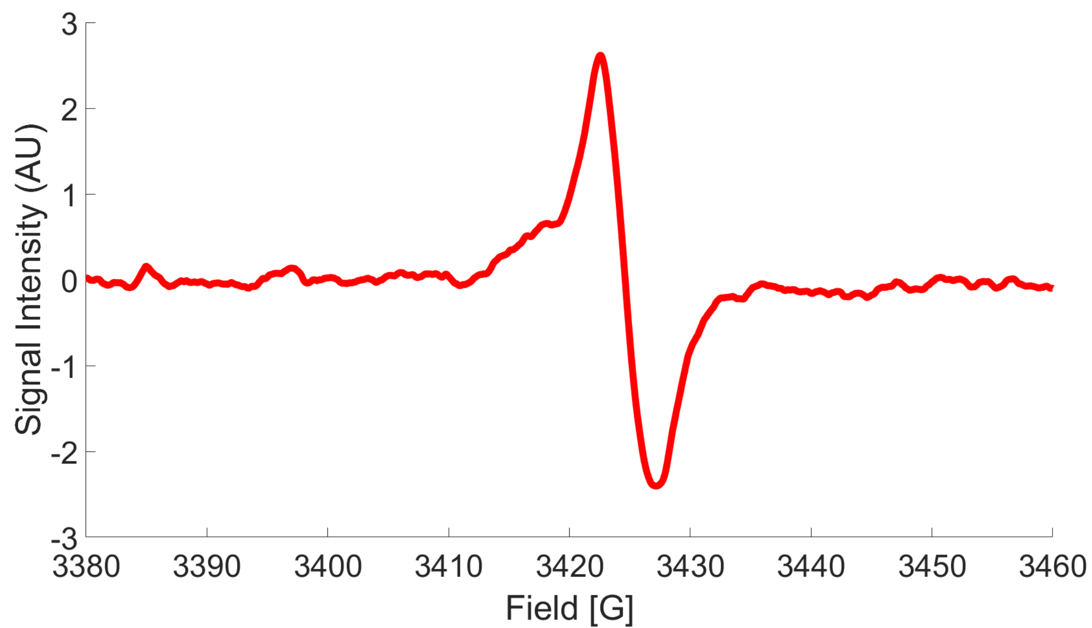

Figure 4.23: Data at $\theta = 165°$ and a modulation frequency of 12,500 Hz.

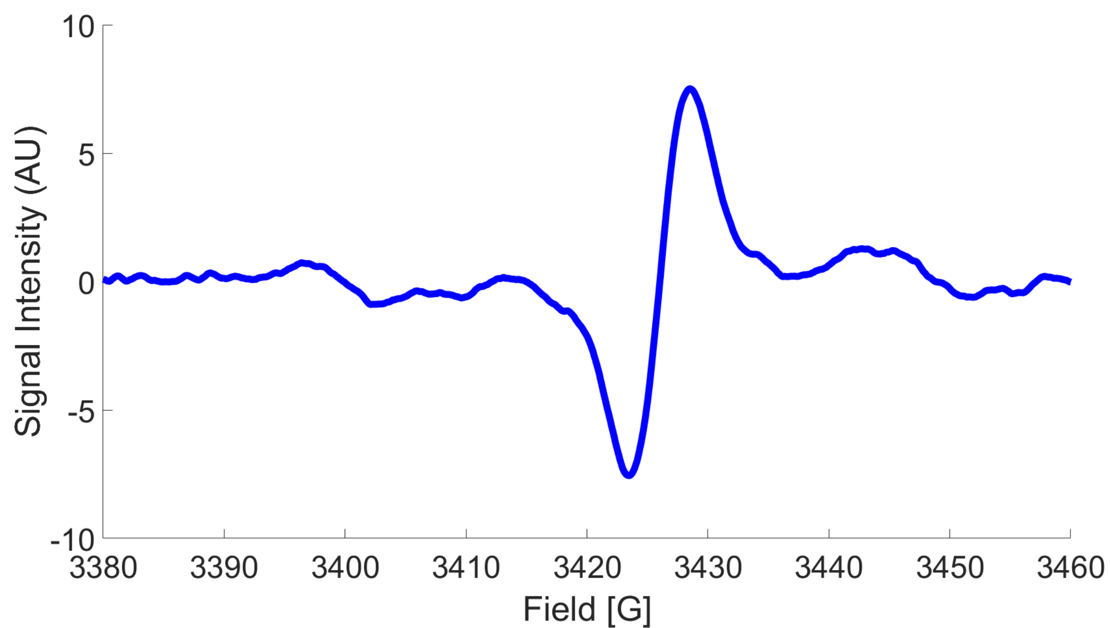

Figure 4.24: Data at $\theta = 165°$ and a modulation frequency of 100 Hz.

Chapter 5

Discussion

5.1 General Discussion

Figure 5.1 maps the g values for both the high modulation and low modulation X-band data. For the high modulation data, the g values range from 2.0048 to 2.0021. Given that the direction normal to the device face is about the crystalline-c axis, g (perpendicular to plane) $= 2.0048$ and g (parallel to plane) $= 2.0035$. The g values demonstrate clear anisotropy and are, in general, consistent with the range of g values reported for nitrogen and nitrogen-related defects in SiC [2, 3, 4, 8, 19]. While the range of values is similar, the exact mapping itself is somewhat inconsistent with reported values. This may be a result of differences in device growth; a three-dimensional g map could help resolve this discrepancy. Unfortunately, the timing of the project in conjunction with the COVID-19 pandemic prevented such data from being available for this work The spread of g values are somewhat consistent with SiC/SiO_2 dangling bonds in SiC MOSFETs [7, 17]. Moreover, dangling bonds at the SiC/SiO_2 interface are not a possibility for the PIN regions not bordering the border oxide (i.e. the region at the JTE is applicable although atypical). Still, even g values for devices

with similar defects in SiC have some variability [7]. Additionally, the g values for the PIN match quantitatively the g values for carbon dangling bonds in one study on a SiC/SiO_2 doubly-diffused MOS device with an oxide grown in N_2O, though the angle is shifted 90° [7]. In that work, $g_\parallel = 2.0051$ and $g_\perp = 2.0029$ [7]. The results for the devices from [7] are depicted in figure 5.2. The g values for the low modulation data drop to lower values that are more similar to values of g reported in literature [2]. The values for angles $\theta = 0°$ to $\theta = 75°$ are similar between datasets but are lower for $\theta > 75°$.

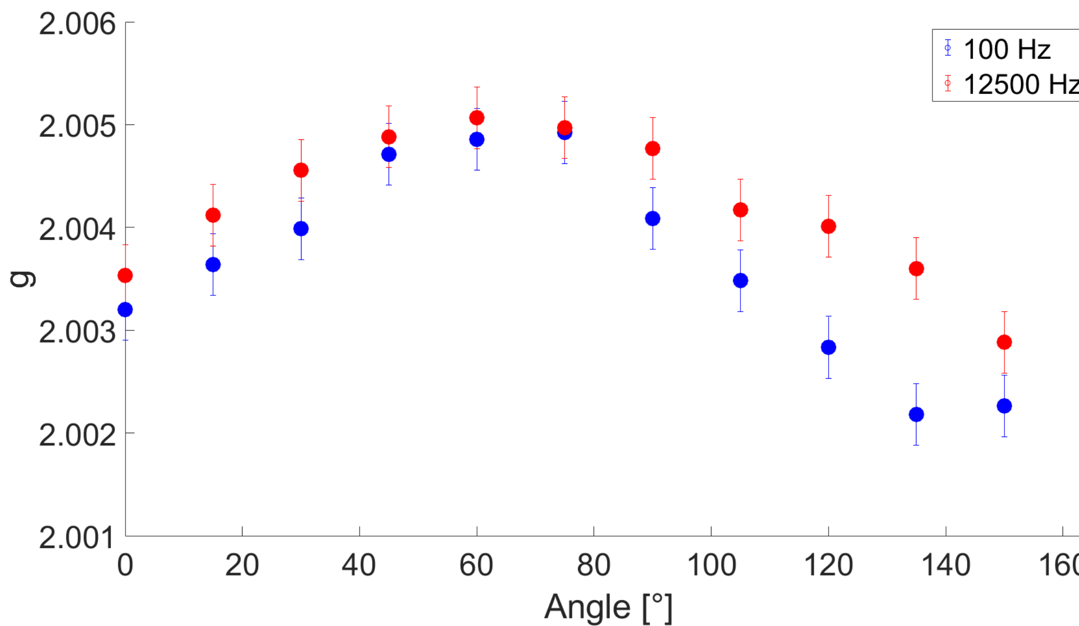

Figure 5.1: Composite figure of all central gs.

The lineshapes of the high modulation and low modulation measurements are significantly different even at the same angle. While the centerlines are, in general, similar besides a difference in signal sign from detection phase, the low modulation data has sidelines which appear similar to hyperfine sidelines. However, the sidelines on the low modulation data vary in shape from the centerline; while the centerline falls and then rises, the sidelines rise and then fall, without accounting for the direction change from the phase. This is different from the lineshapes typically observed for hyperfine interactions [25].

Additionally, the signal amplitudes as a function of angle have been included in figure 5.3. This

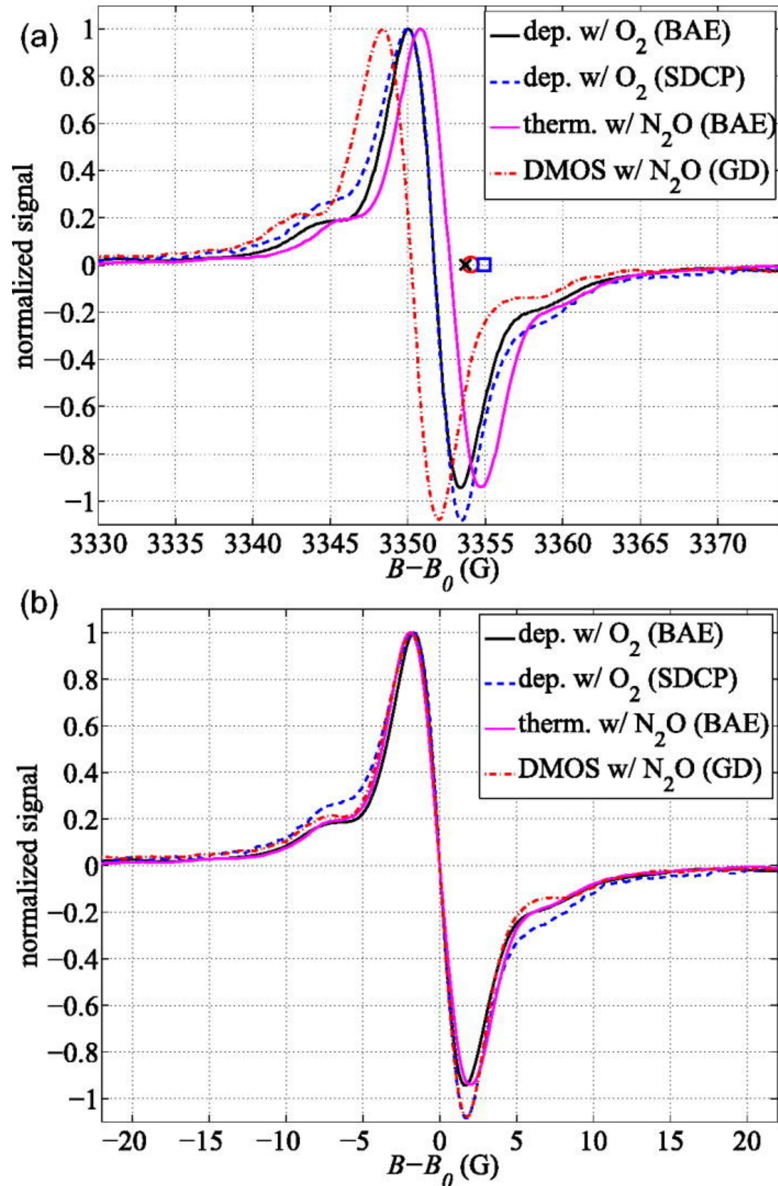

Figure 5.2: EDMR traces from SiC/SiO_2 interfaces in MOS devices. Figure from [7].

is similar to a $\Delta I/I$ plot because the current was held constant at $I = 1.5\mu$A. The amplitude of the 100 Hz data is dramatically larger than the 12,500 Hz data. However, the noise level is also higher. Despite lower signal size, future work might most efficiently utilize high modulation frequencies like 12,500 Hz in order to avoid the sidelines in the low modulation frequency data and to achieve the substantially better signal to noise ratio found in the high modulation frequency traces.

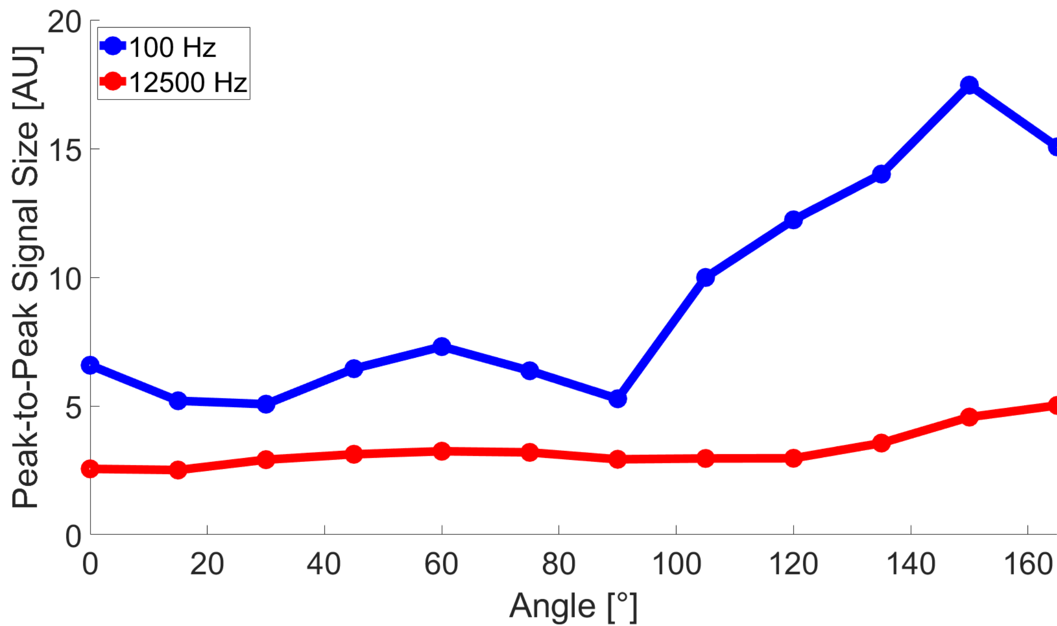

Figure 5.3: Magnitude of the peak-to-peak signal at each angle for each modulation frequency. This plot is inherently normalized by current insofar as the measurements were all taken at the same current, so no further normalization is necessary.

5.2 12,500 Hz

The high modulation data more closely resembles traditional EDMR results. The g values in figure 5.1 likely preclude isolated V_{Si} as the singular dominant defect the PIN diode. Silicon vacancy spectra typically have isotropic $g = 2.003$ [2, 20, 26, 21]. Because the values reported are anisotropic, this defect is potentially eliminated from the pool of possible defects despite its frequency of detection in other SiC diodes [2, 21]. Note that the spin physics of the silicon vacancy is fairly complex [20, 21]. Because of this complexity, it may not be appropriate to completely rule out some role for such defects in these observations.

While the range of g values is somewhat consistent with nitrogen-related defects, the lineshape is not identical to any previously reported nitrogen-related defects. For example, compare figure 4.1 to 2.2a. While the line widths of the centerlines, shape of the left side feature, and relative heights of the left side feature and the centerline are all similar, the signal in figure 4.1 does not have distinctly visible features on the right of the centerline. Moreover, the left side feature in the

high modulation data varied both in exact location relative to the centerline and in relative signal amplitude. The lineshape in figure 2.2 is especially similar to the simulated lineshape for a $N_C V_{Si}^0$ defect [8]. Experimental and simulated spectra for this type of defect are found in figure 5.4.

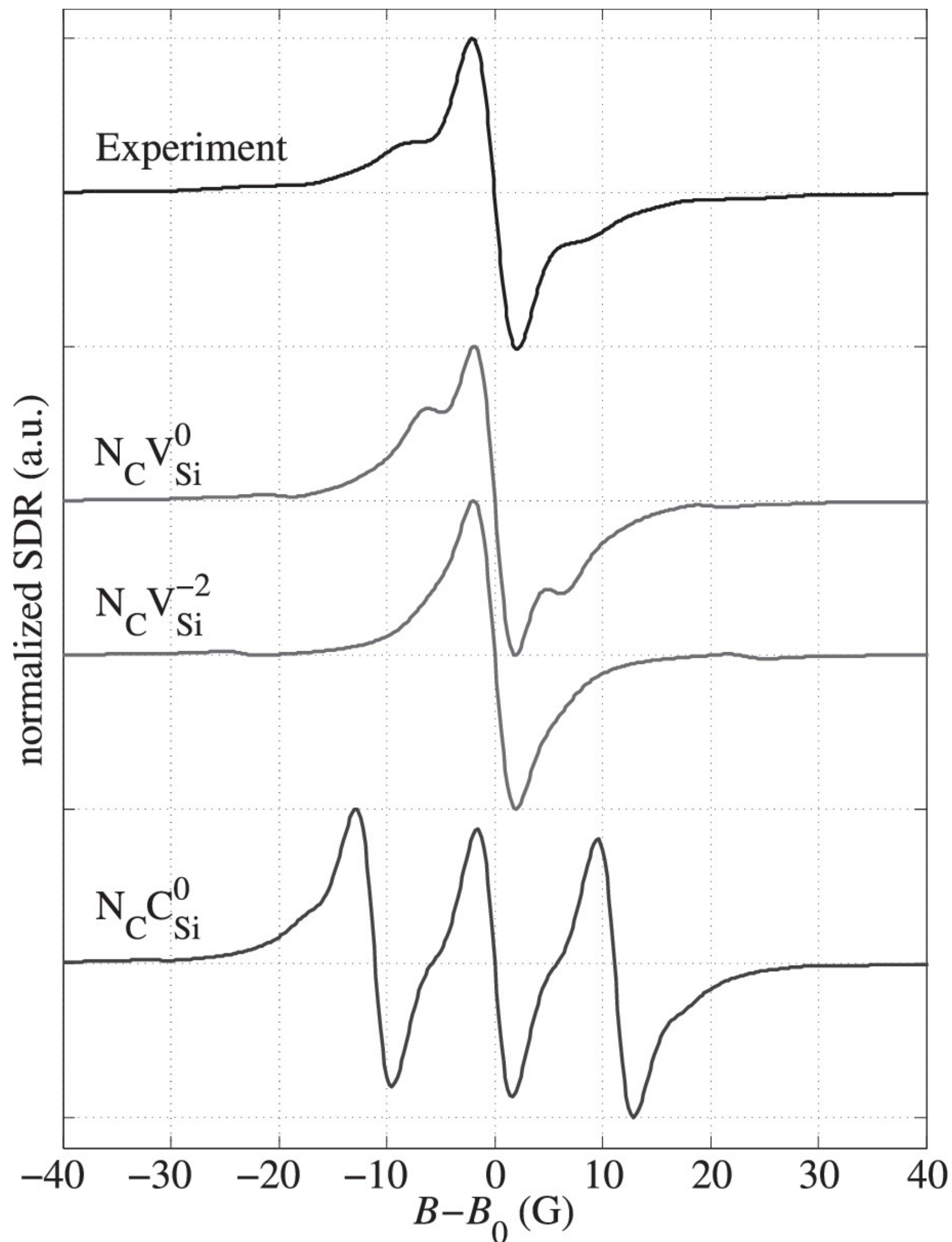

Figure 5.4: Experimental and simulated results for N-related defects in SiC. Figure from [8]

A defect like the $N_C V_{Si}^0$ defect is a plausible candidate for the PIN structure. First, SDR occurs primarily in the depletion region for a diode. For a PIN, this is generally in the intrinsic region.

For this reason, a nearby dopant linked to an intrinsic defect is a plausible candidate. However, the differences between the lineshape of the PIN and what is reported by Aichinger et al. and Cottom et al. do not necessarily support this claim.

Work by Savchenko et al. provides a different possible explanation for the defect. The N_x defect includes coupling by nitrogen at two different lattice sites with a silicon between them [4]. The resulting spectrum, found in figure 2.4, is a Dysonian lineshape made up of a Lorentzian line and a Dysonian line [4]. Something akin to this combination of atypical lineshapes could potentially explain the spectra seen for the PIN diode. Figure 5.5 depicts how the experimental data depicted in figure 4.1 could be created from a Gaussian signal and an approximated Dysonian lineshape.

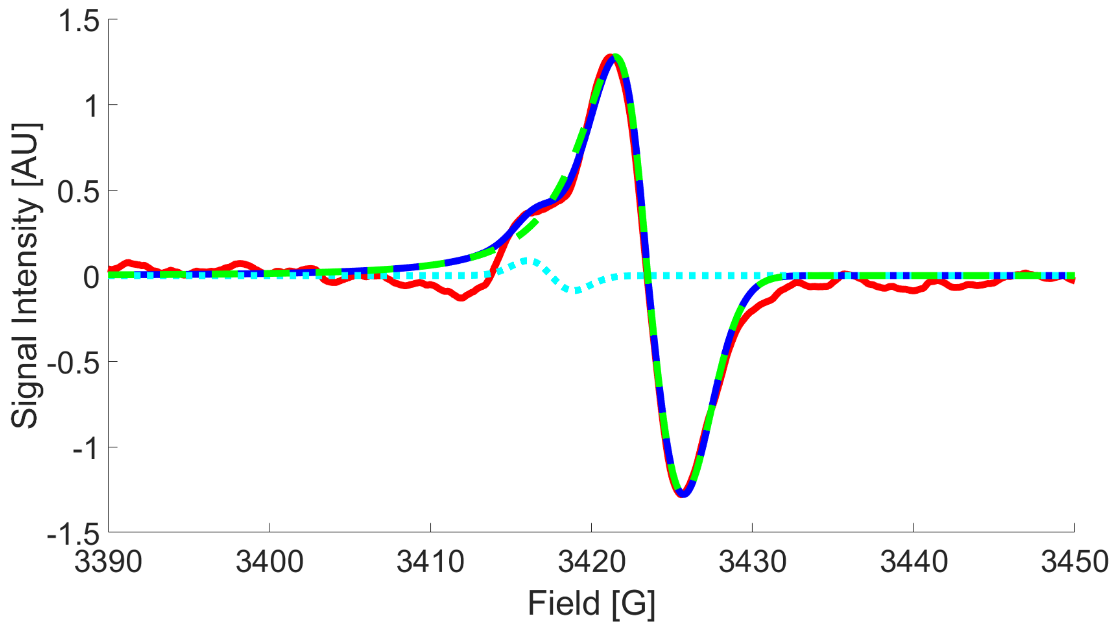

Figure 5.5: 12,500 Hz modulated X band trace on SiC at $\theta = 0°$ with two hypothetical signals combined to recreate the experimental data. The cyan curve is a small, broad Gaussian, whereas the green curve is a Dysonian-like lineshape made from a Lorentzian and a Gaussian signal combined. Note that the green curve is not a Voight line, it is Lorentzian at values of B lower than the zero-crossing and Gaussian at B values higher than the zero-crossing.

The combined signals depicted in figure 5.5 explain several qualitative phenomena. First, a prominent Dysonian-like lineshape fits given the high asymmetry in the centerlines throughout all of the dataset. Second, a smaller line found at a lower magnetic field provides a rationalization for the shifting feature left of the centerline. While the feature appears similar to the side features in

both $N_C V_{Si}^0$ and isolated silicon vacancies at some angles (e. g. $\theta = 0°$), the feature is relatively closer to the centerline near $\theta = 90°$ and forms a somewhat different lineshape (see figure 4.15).

Despite the relatively good fit, there are several major differences between the phenomenon observed by Savchenko et al. and in the PIN diodes. First, the lineshape in Savchenko et al.'s N_x detection does not necessarily include the same side feature left of the centerline. Second, the signal reported by Savchenko et al. broadens and decreases in magnitude as temperature increases; the perpendicular signal at 140 K requires 1600 times multiplication to be on the same scale as the signal at 7 K [4]. Third, the material studied by Savchenko et al. is highly N doped SiC, with $N_D - N_A \approx 10^{19}\text{cm}^{-3}$ [4].

There are nontrivial differences in g values and in lineshape between the results for the PIN diode and most other previously reported results. What is true is that both g and the features in the lineshape are highly anisotropic. The signal identified, however, is well mimicked by combining two lineshapes, one of which is superficially more Dysonian than it is Gaussian or Lorentzian. The Dysonian lineshape is generally associated with nearly metallic regions [4]. The Gaussian and Lorentian lineshapes, however, are typical for standard EPR lines in semiconductors. It is possible, then that the defect involved is near the region in which the n+ region transitions into the intrinsic region or where the intrinsic region meets the p region of the PIN. It is also plausible that more than one defect exists. In this case, there could be a dominating defect near the n+ region, causing the near-Dysonian lineshape, and there could be a less dominating defect in or throughout the intrinsic region.

As noted, the range of g is also similar to that of an interface dangling bond in SiC that could be near either carbon or silicon atoms [7, 17]. The defects could have properties similar to dangling bonds on intrinsic atoms near a donor atom based on the data for a 12,500 Hz modulation frequency. Moreover, only the DMOS device with an oxide grown in N_2O has a lineshape where the right side feature is notably smaller than the left side feature, as depicted in figure 5.2 [7]. The similiaraties between the lineshape of that defect and the PIN as well as the similarities in g values suggest further than they may possess similar or closely-related defects, though the angle

shift disrupts this suggestion. Moreover, this type of defect is unlikely to be found alone within the semiconducting region. As such, it should only be noted as something that could, at best, bear relevance after future investigation. Unfortunately, the signal-to-noise for most traces is too low to make any comments about the potential hyperfine structure for either peak, and so the exact composition of the defects present will require future work. Given the efficacy of low temperature experiments in other works, it is possible that measurements at lower temperatures could likely provide the insight needed to fully identify the defect or defects detected in this work.

5.3 100 Hz

The 100 Hz data is altogether more complicated than the 12,500 Hz data. First, the centerlines have, in many cases, similar structures and side structures to the 12,500 Hz data. The 100 Hz data contains several sidelines which are present near where hyperfine sidelines often occur in EPR measurements. Figure 5.6 depicts the field difference between the ”hyperfine” lines and the zero-crossing for both the 100 Hz and the 12,500 Hz centerlines.

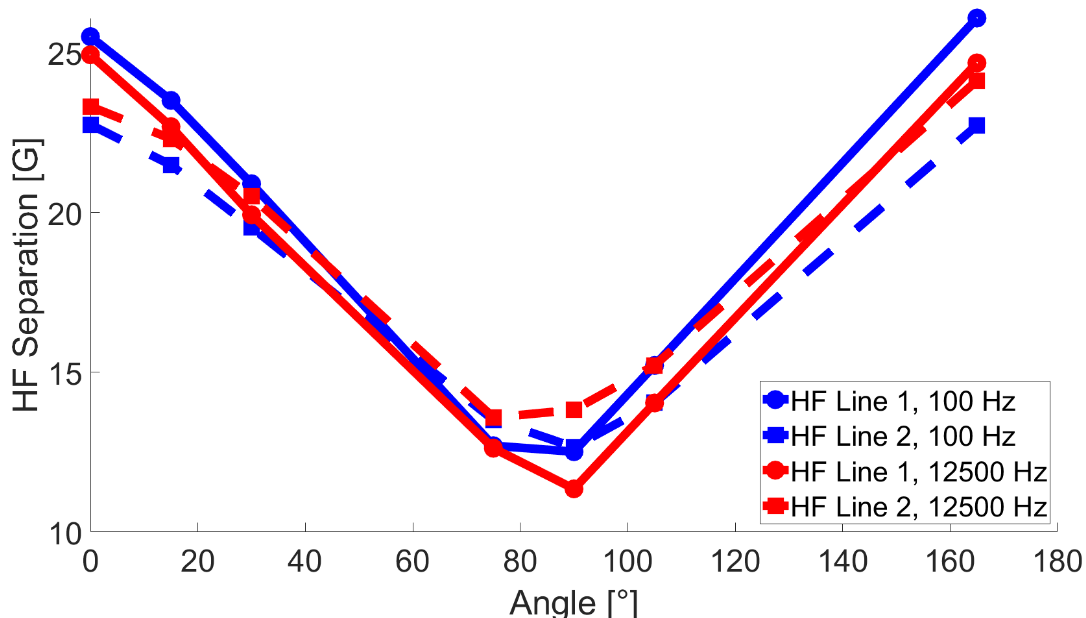

Figure 5.6: Sideline spacing between sidelines in the 100 Hz traces and the zero-crossings of both the 100 Hz and 12,500 Hz centerlines.

From figure 5.6, it is clear that the sidelines are closest around $\theta = 90°$ and farthest at about $90°$ away from $\theta = 90°$. Figure 5.7 depicts the separation from a V_{Si}, given that V_{Si} are especially common in SiC. From the figure, it is clear the sidelines are not symmetric about a V_{Si}. This supports earlier claims that the primary electrically active, spin dependent defected detected is not a single a V_{Si}.

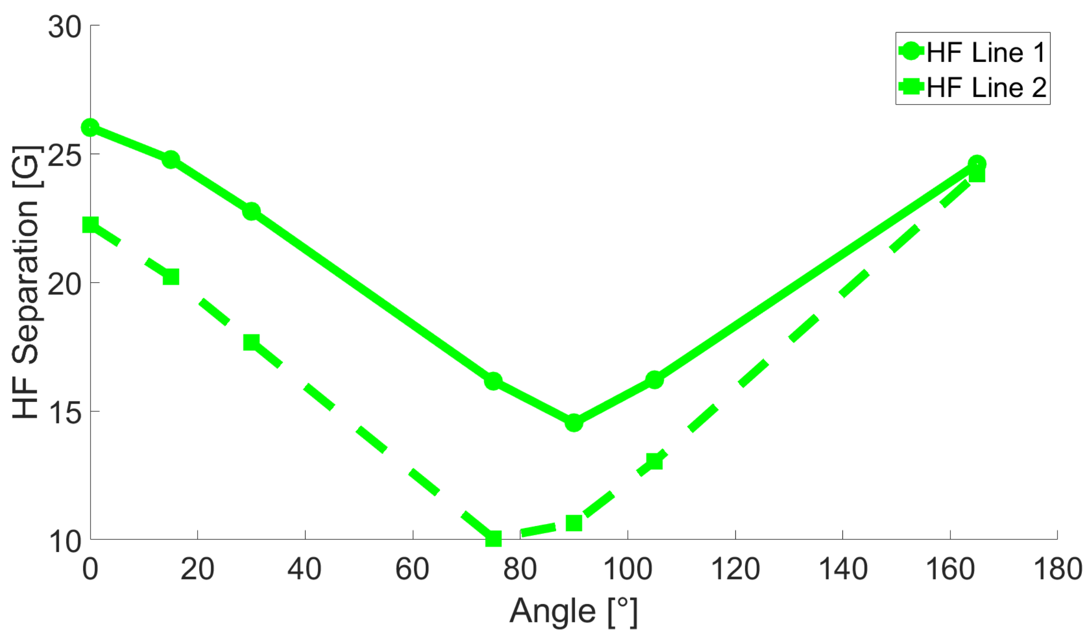

Figure 5.7: Spacing between the hyperfine sidelines and a silicon vacancy, if it were present.

More importantly, the direction of the sidelines is opposite of the centerline. In other words, once phase is accounted for, the current increases and then decreases as it approaches resonance for the centerline, but the current decreases then increases through the sidelines. This is incredibly atypical and is, at best, seldom or never discussed in most EPR literature [11, 13]. For both of these reasons, it is unlikely that the sidelines are hyperfine features. Moreover, the symmetry and opposite direction of the lines likely preclude them from being lines for a defect undetected in the 12,500 Hz scans.

Perhaps the key distinction is that this is an EDMR experiment, rather than a classical EPR experiment, and so the observed spectra includes effects that are almost certainly directly related to the current-mechanisms used by EDMR. If this is the case, than figures 4.2, 4.4, 4.6, 4.12, 4.14,

4.16, 4.22, and 4.24 are likely some of the first evidence for this type of event.

Assuming the centerline signal in both the 100 Hz and 12,500 Hz data is from the same SDR event and assuming the side features are associated with only one defect or defect complex, it may be possible to glean some insight as to what type of defect and spin dependent current mechanism causes the side features. First, consider that the defect is decreasing the current, regardless of current mechanism. For the this to be the case, the defect at resonance is likely decreasing the charge carriers available. This suggests that the defect is likely unlike typical defect structures which increase recombination current in SDR and unlike the line of defects that allow for tunneling through an oxide from one side to another in SDTAT.

Second, the side features only appear in the low modulation frequency data. This time dependence may suggest something about the defect – perhaps long T1 times, or perhaps something about the mechanism. Drawing from the first suggestion, while a line of defects through an oxide is ruled out both because the devices is not an MOS device or capacitor and because the current changes in a way different from SDTAT measurements, it is possible that the defect and charge carrier does involve a tunneling event to a near-edge oxide defect.

A near-edge oxide defect potentially fits both the above conclusions. First, a near-edge oxide defect would likely not increase recombination in the device like a mid-gap defect in the semiconducting material does, which means that it satisfies the current direction. Moreover, it would suggest a decrease in minority charge carriers in the semiconductor material, which could potentially decrease the overall current in the device. Second, it is possible that the high modulation frequency provides too little time for an electron to tunnel to a near-edge oxide defect and then tunnel back, whereas a low modulation frequency may allow enough time for this to occur. In this case, the second condition is satisfied.

Moreover, from figure 3.2, one can see a JTE present on the PIN. This structure is relatively common in PINs. It is possible that some near-edge defects occur as a result of the JTE presence near the oxide. Moreover, the closeness of the side features at near-perpendicular angles closely match defects which would align with the oxide interface.

This line of reasoning is purely speculative and should not be taken as a strict determination for the EDMR results in this work. However, it may be used as a potential guideline for future experiments. For example, it may be useful to fabricate devices with deliberately poor oxides and to determine if the effect is present and if it is more pronounced in such devices. Regardless, further work is needed to elucidate the spin-dependent current mechanisms detected in the 100 Hz dataset in this work.

Chapter 6

Summary and Conclusion

In this work, X-band EDMR measurements were made on SiC PIN diodes at modulation frequencies of 100 Hz and 12,500 Hz. The 12,500 Hz measurements revealed a single line with relatively low signal-to-noise which had an anisotropic range of g values and a slightly asymmetry lineshape that varies in magnitude with angle of rotation. These results did not match closely with any other previously reported spectra; however the range of g values was similar to those reported in multiple devices. The primary defect or defects observed at 12,500 Hz exhibited a range of g that does not match an isolated V_{Si}. The V_{Si} exhibits an isotropic $g = 2.0030 \pm .0003$. They are also different from those of SiC/SiO_2 carbon dangling bonds recently reported for SiC MOSFETs.

The 100 Hz measurements revealed two additional sidelines with characteristics unlike any previously reported EDMR spectra. These results are novel and described a system that includes a defect or defects which increase the SDR current simultaneously with a defect or defects which decrease the current. The additional spectra which is observed at 100 Hz is likely due to a slower process than the recombination event or events which are detected at 12,500 Hz. Though the defect could not be identified, the time dependence, orientation dependence, and difference in current

change suggest that a near-interface defect at the edge of the semiconducting region near the oxide is plausible. In this case, the charge carrier count in the semiconducting region is decreased as charge carriers tunnel to near-interface sites.

Future work should include investigating low-quality SiC/SiO_2 interfaces in PN and PIN diodes.

Bibliography

[1] M. A. Anders, P. M. Lenahan, C. J. Cochrane, and J. van Tol, "Physical nature of electrically detected magnetic resonance through spin dependent trap assisted tunneling in insulators," *Journal of Applied Physics*, vol. 124, no. 21, p. 215105, 2018.

[2] T. Aichinger, P. M. Lenahan, B. R. Tuttle, and D. Peters, "A nitrogen-related deep level defect in ion implanted 4H-SiC PN junctions—a spin dependent recombination study," *Applied Physics Letters*, vol. 100, no. 11, p. 112113, 2012.

[3] N. T. Son, J. Isoya, T. Umeda, I. G. Ivanov, A. Henry, T. Ohshima, E. Janzén, k. o. b. Institutionen för fysik, L. universitet, Halvledarmaterial, and T. högskolan, "EPR and ENDOR studies of shallow donors in SiC," *Applied Magnetic Resonance*, vol. 39, no. 1-2, pp. 49–85, 2010.

[4] D. V. Savchenko, E. N. Kalabukhova, A. Pöppl, E. N. Mokhov, and B. D. Shanina, "EPR study of conduction electrons in heavily doped n-type 4H SiC," *physica status solidi (b)*, vol. 248, no. 12, pp. 2950–2956, 2011.

[5] J. P. Ashton, S. J. Moxim, P. M. Lenahan, C. G. Mckay, R. J. Waskiewicz, K. J. Myers, M. E. Flatte, N. J. Harmon, and C. D. Young, "A new analytical tool for the study of radiation effects in 3-d integrated circuits: Near-zero field magnetoresistance spectroscopy," *IEEE Transactions on Nuclear Science*, vol. 66, no. 1, pp. 428–436, 2019.

[6] B. A. Hull, M. K. Das, J. T. Richmond, J. J. Sumakeris, R. Leonard, J. W. Palmour, and S. Leslie, "A 180 amp/4.5 kv 4H-SiC PIN diode for high current power modules," in *2006 IEEE International Symposium on Power Semiconductor Devices and IC's*, pp. 1–4, 2006.

[7] G. Gruber, J. Cottom, R. Meszaros, M. Koch, G. Pobegen, T. Aichinger, D. Peters, and P. Hadley, "Electrically detected magnetic resonance of carbon dangling bonds at the Si-face 4H-SiC/SiO2 interface," *Journal of Applied Physics*, vol. 123, no. 16, p. 161514, 2018.

[8] J. Cottom, G. Gruber, P. Hadley, M. Koch, G. Pobegen, T. Aichinger, and A. Shluger, "Recombination centers in 4H-SiC investigated by electrically detected magnetic resonance and ab initio modeling," *Journal of Applied Physics*, vol. 119, no. 18, p. 181507, 2016.

[9] X. She, A. Q. Huang, . Lucía, and B. Ozpineci, "Review of silicon carbide power devices and their applications," *IEEE Transactions on Industrial Electronics*, vol. 64, no. 10, pp. 8193–8205, 2017.

[10] D. Planson, A. Henry, N. Thierry-Jebali, E. Janzén, F. Laariedh, S. Scharnholz, P. Brosselard, J. Hassan, B. Vergne, G. Civrac, and M. Lazar, "600 v PIN diodes fabricated using on-axis 4H silicon carbide," *Materials science forum*, vol. 717-720, pp. 969–972, 2012.

[11] P. Bertrand and S. O. service), *Electron Paramagnetic Resonance Spectroscopy: Fundamentals*. Cham: Springer International Publishing, 1st 2020. ed., 2020.

[12] J. A. Weil, J. R. Bolton, and W. I. O. service), *Electron paramagnetic resonance: elementary theory and practical applications*. Hoboken, N.J: Wiley-Interscience, 2nd ed., 2007.

[13] D. Goldfarb and S. Stoll, *EPR Spectroscopy: Fundamentals and Methods*. Newark: John Wiley & Sons, Incorporated, 2018.

[14] M. A. Anders, P. M. Lenahan, and A. J. Lelis, "Multi-resonance frequency spin dependent charge pumping and spin dependent recombination - applied to the 4H-SiC/SiO2 interface," *Journal of Applied Physics*, vol. 122, no. 23, p. 234503, 2017.

[15] M. A. Anders, P. M. Lenahan, A. H. Edwards, P. A. Schultz, R. M. Van Ginhoven, and N. U. S. Sandia National Lab. (SNL-NM), Albuquerque, "Effects of nitrogen on the interface density of states distribution in 4H-SiC metal oxide semiconductor field effect transistors: Super-hyperfine interactions and near interface silicon vacancy energy levels," *Journal of Applied Physics*, vol. 124, no. 18, p. 184501, 2018.

[16] C. J. Cochrane, P. M. Lenahan, and A. J. Lelis, "Identification of a silicon vacancy as an important defect in 4H SiC metal oxide semiconducting field effect transistor using spin dependent recombination," *Applied Physics Letters*, vol. 100, no. 2, p. 023509, 2012.

[17] D. J. Meyer, P. M. Lenahan, and A. J. Lelis, "Observation of trapping defects in 4H–silicon carbide metal-oxide-semiconductor field-effect transistors by spin-dependent recombination," *Applied Physics Letters*, vol. 86, no. 2, p. 023503, 2005.

[18] C. J. Cochrane, P. M. Lenahan, K. Matocha, A. J. Lelis, J. Fronheiser, and B. C. Bittel, "EDMR and EPR studies of 4H SiC MOSFETs and capacitors," *Materials Science Forum*, vol. 645-648, pp. 527–530, 2010.

[19] J. Isoya, N. Morishita, T. Ohshima, K. Fukuda, T. Umeda, R. Kosugi, and K. Esaki, "Electrically detected magnetic resonance (EDMR) studies of SiC-SiO2 interfaces," *Materials Science Forum*, vol. 717-720, pp. 427–432, 2012.

[20] C. J. Cochrane, P. M. Lenahan, and A. J. Lelis, "An electrically detected magnetic resonance study of performance limiting defects in SiC metal oxide semiconductor field effect transistors," *Journal of Applied Physics*, vol. 109, no. 1, pp. 014506–014506–12, 2011.

[21] C. J. Cochrane, H. Kraus, P. G. Neudeck, D. Spry, R. J. Waskiewicz, J. Aston, and P. M. Lenahan, "Magnetic field sensing with 4H SiC diodes: n vs p implantation," *Materials Science Forum*, vol. 924, pp. 988–992, 06 2018. Copyright - Copyright Trans Tech Publications Ltd. Jun 2018; Last updated - 2020-02-26.

[22] A. L. Shluger, G. Pobegen, J. Cottom, G. Gruber, and T. Aichinger, "Identifying performance limiting defects in silicon carbide PN-junctions: A theoretical study," *Materials science forum*, vol. 858, pp. 257–260, 2016.

[23] D. Savchenko, A. Pöppl, E. N. Kalabukhova, S. Greulich-Weber, E. Rauls, W. G. Schmidt, and U. Gerstmann, "Spin-coupling in heavily nitrogen-doped 4H-SiC," in *Silicon Carbide and Related Materials 2008*, vol. 615 of *Materials Science Forum*, pp. 343–346, Trans Tech Publications Ltd, 7 2009.

[24] T. A. G. Eberlein, R. Jones, and P. R. Briddon, "$\mathrm{z}_1/\mathrm{z}_2$ defects in $4H-\mathrm{SiC}$," *Phys. Rev. Lett.*, vol. 90, p. 225502, Jun 2003.

[25] M. Brustolon and G. Giamello, *Electron paramagnetic resonance: a practitioner's toolkit*. Hoboken, N.J: Wiley, 1. aufl. ed., 2009.

[26] T. Sato, H. Yokoyama, and H. Ohya, "Electrically detected magnetic resonance (EDMR) measurements of bulk silicon carbide (SiC) crystals," *Chemistry Letters*, vol. 35, no. 12, pp. 1428–1429, 2006.